First-principles study of $(Ba,Ca)TiO_3$ and $Ba(Ti,Zr)O_3$ solid solutions

Danila Amoroso,[1,2] Andrés Cano,[2] and Philippe Ghosez[1]
[1]*Physique Théorique des Matériaux, Q-MAT, CESAM, Université de Liège (B5), B-4000 Liège, Belgium*
[2]*ICMCB, CNRS, Université de Bordeaux, UMR 5026, F-33600 Pessac, France*

(Received 2 February 2018; revised manuscript received 25 April 2018; published 29 May 2018)

$(Ba,Ca)TiO_3$ and $Ba(Ti,Zr)O_3$ solid solutions are the building blocks of lead-free piezoelectric materials that attract a renewed interest. We investigate the properties of these systems by means of first-principles calculations, with a focus on the lattice dynamics and the competition between different ferroelectric phases. We first analyze the four parent compounds in order to compare their properties and their different tendency towards ferroelectricity. The core of our study is systematic characterization of the binary systems $(Ba,Ca)TiO_3$ and $Ba(Ti,Zr)O_3$ within both the virtual crystal approximation and direct supercell calculations. In the case of Ca doping, we find a gradual transformation from *B*-site to *A*-site ferroelectricity due to steric effects that largely determines the behavior of the system. In the case of Zr doping, in contrast, the behavior is eventually dominated by cooperative Zr-Ti motions and the local electrostatics. In addition, our comparative study reveals that the specific microscopic physics of these solids sets severe limits to the applicability of the virtual crystal approximation for these systems.

DOI: 10.1103/PhysRevB.97.174108

I. INTRODUCTION

Piezoelectric devices have successfully relied on lead zirconate titanate (PZT) materials for several decades. Since 2003, the European Union has restricted the use of certain hazardous substances [1], such as Pb, which has driven the search for alternative lead-free piezoelectric compounds. In this respect, $BaTiO_3$-based solid solutions appear as interesting candidates, whose potential for piezoelectric applications has been known since the sixties [2,3]. Among possible combinations, the partial homovalent substitution of Ba by Ca and Ti by Zr at the *A* and *B* sites of $BaTiO_3$ ($Ba_{1-x}Ca_xTi_{1-y}Zr_yO_3$ hereafter BCTZ) is of special interest. In their seminal paper, Liu and Ren [4] reported a high piezoelectric coefficient of 620 pC/N for the ceramic system $(Ba_{0.7}Ca_{0.3})O_3$-$Ba(Ti_{0.8}Zr_{0.2})O_3$. This has been ascribed to the presence of a special point in the phase diagram in which the tetragonal and rhombohedral ferroelectric phases meet the paraelectric cubic one. Subsequently, Keeble *et al.* [5] revisited this phase diagram and observed an intermediate ferroelectric orthorhombic phase that also meets the three previous ones.

As in the case of Pb-based systems, the achievement of high piezoelectric response in BCTZ is believed to be linked to the existence of a so-called phase convergence region, in which the lack of an energy barrier between different ferroelectric states makes the landscape isotropic and the polarization free to rotate [6]. However, no theoretical confirmation of this picture has been provided yet for this system. In fact, although a large number of experimental studies have been reported [4,5,7,8], the number of theoretical investigations of BCTZ compounds remain comparatively very limited and, to the best of our knowledge, no comprehensive study based on direct density functional theory (DFT) has been carried out so far.

In order to fill in this gap, here we report a systematic first-principles DFT study of $(Ba,Ca)(Ti,Zr)O_3$-type compounds with the intend to clarify the evolution with composition of their ferroelectric, piezoelectric, and related properties. We proceed step by step. Thus we first address carefully the four parent compounds. Then, starting from $BaTiO_3$, we investigate separately the evolution of the properties in $(Ba,Ca)TiO_3$ and $Ba(Ti,Zr)O_3$ solid solutions in order to disentangle the role of individual atomic substitutions at the *A* and *B* sites. We use both the virtual crystal approximations (VCA) and explicit ordered supercells of different compositions. In each case, starting from the reference high-symmetry paraelectric phase, we identify and characterize the existing phonon instabilities. Then, comparing the energy of various possible distorted phases obtained from the condensation of unstable modes, we search and characterize the structural ground state. All along this work, a special emphasis is put on the analysis of the real-space interatomic force constants in order to rationalize the evolution of the properties with composition. Through such quantitative analysis and comparisons of properties between the parent compounds and their related solid solutions, our work reveals the distinct underlying microscopic mechanisms activated by *A*- and *B*-site atomic substitutions. At the same time, it points out and explains strong limitations of the VCA approach for the $(Ba,Ca)TiO_3$ and $Ba(Ti,Zr)O_3$ systems.

The paper is organized as follows. In Sec. II, we introduce the technical details of our DFT calculations. Then, in Sec. III, we carefully analyze the four parent compounds. Next, in Secs. IV and V, we address separately $(Ba,Ca)TiO_3$ and $Ba(Ti,Zr)O_3$ solid solutions of different compositions. Finally, Secs. VI and VII are devoted to a global discussion and the conclusions respectively.

II. TECHNICAL DETAILS

A. Computational details

We use the general framework of the density functional theory (DFT) to compute the structural properties and the electric polarization. Dynamical and piezoelectric properties have been calculated using density functional perturbation theory (DFPT)

TABLE I. Relaxed lattice parameter a_{cell} (in angstrom) of the cubic structure of the four parent compounds. Experimental values are also reported for comparison.

	$BaTiO_3$	$CaTiO_3$	$BaZrO_3$	$CaZrO_3$
Present	3.975	3.840	4.184	4.099
Exp.	4.003 [18]	3.897 [20]	4.191 [19]	4.020 [21]

[10], as implemented in the ABINIT package [11–13]. The exchange-correlation potential was evaluated within the generalized gradient approximation (GGA) using the Wu-Cohen (WC) functional [14] for all simulations. Optimized norm-conserving pseudopotentials [15] have been employed with the following orbitals considered as the valence states: $5s$, $5p$, and $6s$ for Ba, $3s$, $3p$, and $4s$ for Ca, $3s$, $3p$, $4s$, and $3d$ for Ti, $4s$, $4p$, $4d$, and $5s$ for Zr, and $2s$ and $2p$ for O. The energy cutoff for the expansion of the electronic wave functions has been fixed to 45 Ha. Before performing computationally demanding calculations on ordered supercells by using a standard DFT approach, a first investigation has been performed using the VCA, which relies on virtual atoms obtained from combination of the reference atomic pseudopotentials [16,17]. For the optimization of the cubic pervoskite structures, phonons and polarization calculations within VCA, we used a $6 \times 6 \times 6$ k-point mesh for the Brillouin zone sampling for which energy is converged to 0.5 meV. For the optimization of the polar $P4mm$, $R3m$, and $Amm2$ and piezoelectric response calculations, different sampling from $8 \times 8 \times 8$ to $8 \times 6 \times 6$ were used. For the optimization of the supercells and for the associated phonons calculations we used the $8 \times 8 \times 8$ k-mesh. For all the tetragonal superlattices, we used $8 \times 8 \times 6$ k-mesh sampling. In order to allow comparison between different structures, energy will be reported in meV/f.u. (i.e., per 5 atoms). The q points for the phonon dispersion curves and IFCs of the four pure compounds included Γ, X, M, R, and the Λ point halfway from Γ to R of the simple cubic Brillouin zone.

B. Structure of the parent compounds

The optimized lattice parameters of the cubic structure of the four parent compounds are reported in Table I. There, the atoms in the ABO_3 perovskite structure are labeled according to Fig 1. These values are used in Sec. III A for the calculation of the phonon dispersion curves and interatomic force constants. The obtained values are in excellent agreement with experimental data for $BaTiO_3$ and $BaZrO_3$ [18,19] (within 1%), whereas for $CaTiO_3$ the underestimation is of about 2% [20]. The larger error for $CaTiO_3$ can be assigned to the fact that the 0 K DFT results are compared to measurements at 1720 K. For $CaZrO_3$, the optimized lattice parameter overestimates the experimental value [21] of about 2%.

C. Supercell structures

We have considered different supercells describing the Ca and Zr doping of $BaTiO_3$ and performed DFPT calculations on the corresponding relaxed high-symmetry paraelectric structures. For $Ba_{7/8}Ca_{1/8}TiO_3$ and $BaTi_{7/8}Zr_{1/8}O_3$, we have used the smallest reference structure, which is the cubic $Pm\bar{3}m$ (O_1^h)

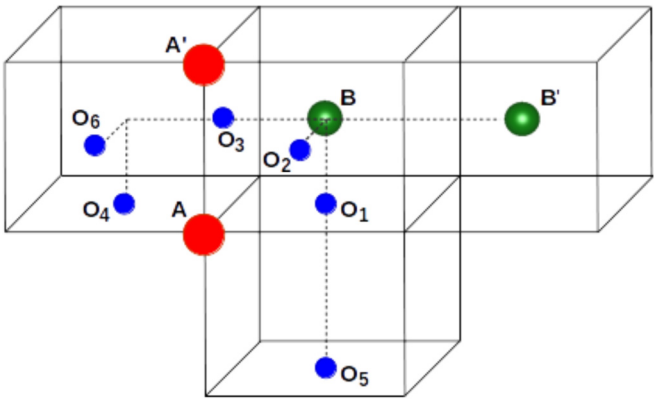

A	(0.0, 0.0, 0.0)	A'	(0.0, 0.0, 1.0)
B	(0.5, 0.5, 0.5)	B'	(1.5, 0.5, 0.5)
O_1	(0.5, 0.5, 0.0)	O_4	(-0.5, 0.5, 0.0)
O_2	(0.5, 0.0, 0.5)	O_5	(0.5, 0.5, -1.0)
O_3	(0.0, 0.5, 0.5)	O_6	(-0.5, 0.0, 0.5)

FIG. 1. (Top) Schematic 3D view of atoms. (Bottom) Positions in reduced coordinates of the atoms in the perovskite structure.

with 40 atoms. The GGA-WC optimized lattice constants are 7.917 and 8.003 Å, respectively (Fig. 2).

For $Ba_{0.50}Ca_{0.50}TiO_3$ and $BaTi_{0.50}Zr_{0.50}O_3$, three distinct geometric arrangements of the 40-atom cell were considered: columns of same cations along the [001] direction, layers of same cations parallel to the [110] planes and rocksalt configuration, Fig. 2. The paraelectric reference of the two first "ordered" structures are characterized by a tetragonal symmetry within the $P4/mmm$ (D_1^{4h}) space group and they can be reduced by symmetry to 10-atom cell, whereas the rocksalt configuration has the cubic symmetry within the $Fm\bar{3}m$ (O_5^h) space group. Structural relaxation have been done on the $2 \times 2 \times 2$ supercells (40 atoms) for each geometrical ordering, whereas DFPT calculations and structural relaxation of lower symmetry structures have been performed on the reduced 10-atom cell for the $P4/mmm$ structures and on the 40-atom cell for the $Fm\bar{3}m$ one. The optimized lattice parameters of the high-symmetry references are reported in Table II. Figures have been produced by using the VESTA package [73].

TABLE II. Optimized lattice parameters (in angstrom) of the tetragonal $P4/mmm$ and the cubic-$Fm\bar{3}m$ structures for $Ba_{0.50}Ca_{0.50}TiO_3$ and $BaTi_{0.50}Zr_{0.50}O_3$ solid solutions. For the tetragonal $P4/mmm$, we report values related to the reduced 10-atom cell. The relations with respect to the $2 \times 2 \times 2$ supercell are (columnar) $a = b = a_{(2\times2\times2)}/\sqrt{2}$ and $c = c_{(2\times2\times2)}/2$, (layered) $a = b = a_{(2\times2\times2)}/2$ and $c = c_{(2\times2\times2)}$.

Structure		$Ba_{0.50}Ca_{0.50}TiO_3$	$BaTi_{0.50}Zr_{0.50}O_3$
$P4/mmm$	columnar [001]	$a = b = 5.535$ $c = 3.899$	$a = b = 5.752$ $c = 4.104$
	layered [110]	$a = b = 3.911$ $c = 7.803$	$a = b = 4.098$ $c = 8.125$
$Fm\bar{3}m$		$a = b = c = 7.825$	$a = b = c = 8.150$

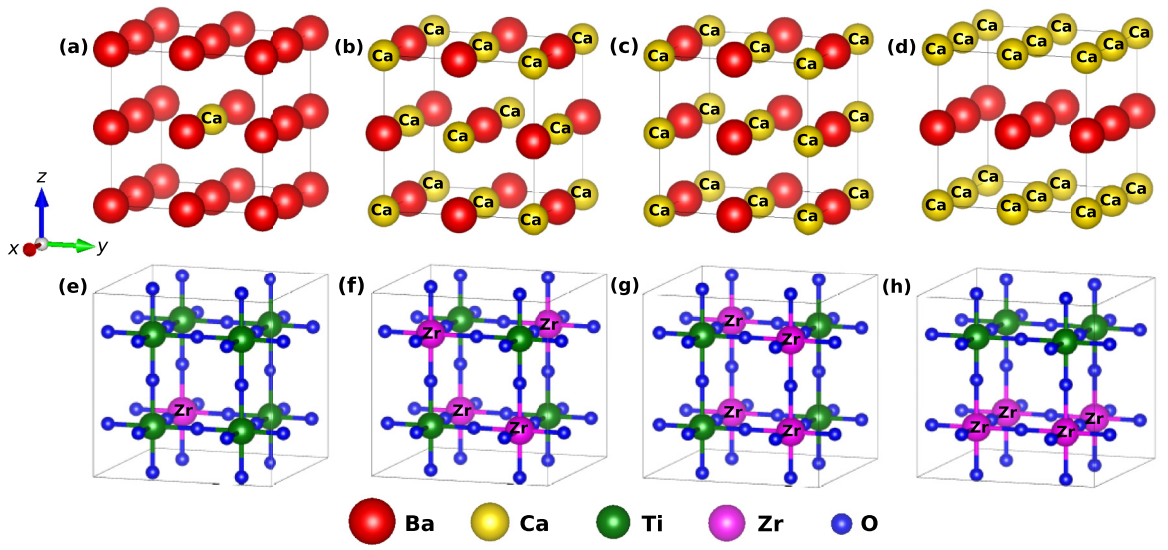

FIG. 2. Schematic representation of different atomic ordering in $2 \times 2 \times 2$ supercells for the two investigated solid solutions. (Top) Sublattice of A cations in $Ba_{1-x}Ca_xTiO_3$. (Bottom) Sublattice of B cations and oxygens in $BaTi_{1-y}Zr_yO_3$. Ca and Zr atoms are labeled to help the visualization. [(a) and (e)] $x, y = 0.125$. [(b) and (f)] rocksalt order, [(c) and (g)] columnar order along the z axis, and [(d) and (h)] layered order perpendicular to z axis for $x, y = 0.50$.

III. PARENT COMPOUNDS

We start our study by considering individually the $BaTiO_3$, $CaTiO_3$, $CaZrO_3$, and $BaZrO_3$ parent compounds. The dynamics and the energetics of these systems is fundamental to understand the key features of the related solid solutions.

$BaTiO_3$ is one of the most studied perovskite, both from the theoretical [22–26] and experimental [27–29] points of view. This perovskite is characterized by a tolerance factor t greater than 1, $t \simeq 1.06$ [30], that allows to predict a polar distorted ground state [30]. In fact, while stable at high temperature in the centrosymmetric cubic ($Pm\bar{3}m$) phase, it undergoes [29] ferroelectric structural phase transitions to a tetragonal ($P4mm$) structure at $\simeq$393 K, to a orthorhombic ($Amm2$) phase at $\simeq$278 K, and to a rhombohedral ($R3m$) ground state at 183 K.

$CaTiO_3$, on the contrary, has a tolerance factor t smaller than 1, $t \simeq 0.97$ [30]. Accordingly, this compound displays a nonpolar orthorhombic ($Pnma$) ground state. It exhibits at least two observed phase transitions at high temperatures: from a cubic ($Pm\bar{3}m$) to a tetragonal phase ($I4/mcm$) at $\simeq$1634 K and from a tetragonal ($I4/mcm$) to the orthorhombic ground state ($Pnma$) at $\sim$1486 K [20,31,32].

$CaZrO_3$, that has $t \simeq 0.91$, was observed only in two different structures: the high-temperature cubic ($Pm\bar{3}m$) form and its orthorhombic ($Pnma$) ground state with the transition temperature at $\simeq$2170 K [33–35].

$BaZrO_3$, with $t \simeq 1.00$ [30], is experimentally not known to undergo any structural phase transition and remains in the paraelectric cubic phase down to 2 K [19].

In Sec. III A, we provide a comparison of the dynamical properties (phonon dispersion curves and interatomic force constants) of the parent compounds in their cubic phase. Then, in Sec. III B, we compare the energetics of various metastable phases of lower symmetry arising from the condensation of individual and combined distortions related to the unstable phonon modes identified in Sec. III A.

A. Phonon dispersion curves and interatomic force constants

The identification of imaginary phonon frequencies and the corresponding displacement patterns allow us to pinpoint the main instabilities behind the structural phase transitions in our systems. Thus we considered the cubic reference structure and we computed the phonon dispersion curves along selected high-symmetry lines in the simple Brillouin zone. The results are shown in Fig. 3. The presence of imaginary phonon frequencies (shown as negative values in Fig. 3) reveals the structural instabilities of the cubic phase. The nature of the corresponding transition is usually determined by the character of the main unstable modes and the related eigendisplacement vectors indicate the atomic displacements that spontaneously appear to reach the most stable configuration.

We complement this analysis with the calculation of the interatomic force constants in real space. These constants are defined as $C_{k\alpha,k'\beta}(l,l') = \partial^2 E_{\text{tot}}/\partial\tau^l_{k\alpha}\partial\tau^{l'}_{k'\beta}$, where E_{tot} is the total energy of a period crystal and $\tau^l_{k\alpha}$ is the displacement of the atom k in the cell l along direction α from its equilibrium position. For a pair of distinct atoms, the IFC can be interpreted as minus the harmonic spring constant between them, so that negative values correspond to stable interactions. For the "on-site" forces, on the contrary, positive values correspond to stable interactions. In our analysis, we further separate the distinct contributions coming from the dipole-dipole interaction (DD) and from the short-range forces (SR) in order to identify the key mechanisms that lead the system to display or not specific phonon instabilities. For a more detailed description of the physical meaning and its practical implementation see Refs. [10,36,37]. In the following, we address a systematic

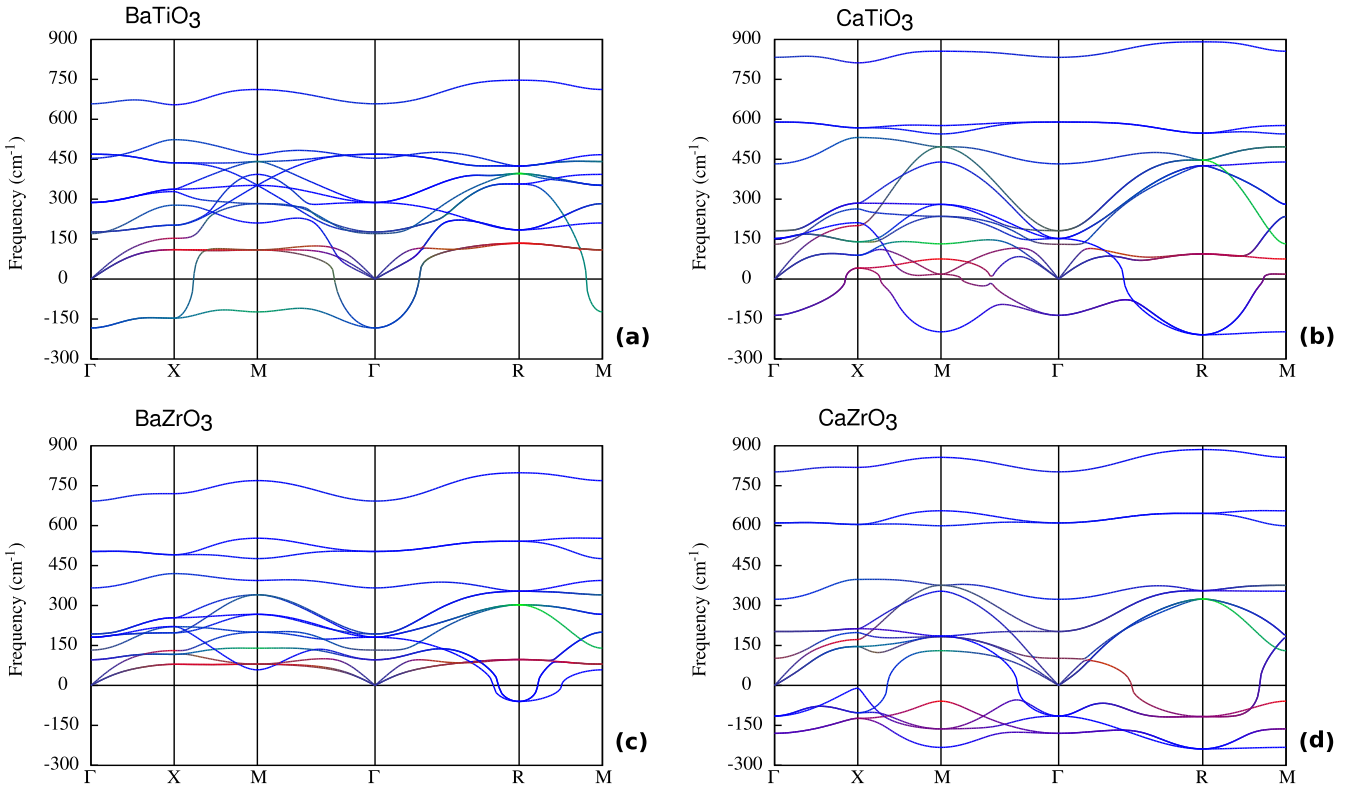

FIG. 3. Calculated phonon dispersion curves of $BaTiO_3$ (a), $CaTiO_3$ (b), $BaZrO_3$ (c), and $CaZrO_3$ (d) along different high-symmetry lines in the simple cubic Brillouin zone. Negative values of frequencies refer to imaginary frequencies (ω are in cm^{-1}). The different colors indicate the different atomic contributions in the corresponding eigenvectors as in Ref. [9] (red for the A atom, green for B atom and blue for O atoms).

description of the phonon dispersion curves reproduced in Fig. 3.

1. $BaTiO_3$

Ferroelectricity in $BaTiO_3$ is known to be related to the Ti off-centering driven by an unstable polar mode at Γ [9,25]. This ferroelectric (FE) instability is such that it expand over the entire Γ-X-M planes of the simple cubic Brillouin zone, as can be seen in Fig. 3(a). While each atom is at a position stable against individual displacements (Table IV), the origin of this distortion has to be primarily ascribed to the destabilizing Ti-O interaction, reflected in the positive value of the interatomic force constant along the bond's direction (Table V). An additional contribution comes from the strong interaction of subsequent Ti-atoms along the B-B' chain direction compared to the small value in the transverse component. These anisotropic couplings give rise to a branch of unstable modes almost flat in the Γ-X-M plane and highly dispersive along Γ-R. This reflects the chain-like nature of the instability in real space. The polar distortion requires cooperative atomic displacement along Ti-O chains [25]. Furthermore, the negligible contribution of Ba atom to the ferroelectric distortion, has to be ascribed to its sizable on-site force constant and very weak Ba-O_1 coupling.

In Table III, we also compare the eigendisplacements associated to the unstable $F_{1u}(TO_1)$ mode to those of the stable $F_{1u}(TO_2)$ and $F_{1u}(TO_3)$ ones and we report the related mode effective charges, as described in Ref. [10]. The mode effective charge is giant for the unstable mode in comparison to the others [36,38]. In fact, the very anomalous Born effective charges on Ti and $O_\parallel$ combined through the specific pattern of eigendisplacements associated to the TO_1 mode in order to produce a large spontaneous polarization, while for the TO_2 and TO_3 modes, the motions are coupled so that Ti and O generate polarizations that partly compensate.

2. $CaTiO_3$

$CaTiO_3$ displays two main nonpolar instabilities at the R and M points of the cubic Brillouin zone related to antiferrodistortive (AFD) motions ($\omega \simeq 209$i and $\simeq 198$i cm^{-1}, respectively). These correspond to cooperative rotations of oxygen octahedron, around the B atoms, with consecutive octahedron along the rotation axis being in-phase at M ($a^0a^0c^+$ in Glazer's notation [39]) and antiphase at R ($a^0a^0c^-$). As such, the M instability appearing in the phonon spectrum is a continuation of the instability at R, while in $BaTiO_3$ it is a continuation of the polar instability at Γ. A detailed description of such AFD instabilities is reported in Ref. [40].

In addition, there is an unstable mode at the Γ point that is also polar. This FE instability is now restricted to a region around the Γ point highlighting a larger and more isotropic ferroelectric correlation volume. This mode enables the condensation of a polar distortion. However, the character of the corresponding ferroelectricity is rather different compared to that in $BaTiO_3$ where it is dominated by the Ti displacements (B-site ferroelectricity). In fact, in $CaTiO_3$, this instability

TABLE III. Born effective charges (in $|e|$) of individual atoms in each parent compound followed by the frequencies, mode effective charges and eigendisplacements ($\langle\eta|M|\eta\rangle = 1$ with M in amu), of F_{1u}(TO) phonon modes at Γ on the optimized cubic phase (Table I). The mode effective charge is defined as in Ref. [10], $\bar{Z}^*_{\rm TO} = |\frac{\sum_{k,\beta} Z^*_{k,\alpha\beta}\eta^{\rm TO}_{k,\beta}}{\sqrt{\langle\eta^{\rm TO}|\eta^{\rm TO}\rangle}}|$.

	$BaTiO_3$	$CaTiO_3$	$BaZrO_3$[a]	$CaZrO_3$
Atom		Born effective charge Z^*		
$A^{(+2)}$	2.751	2.575	2.732	2.623
$B^{(+4)}$	7.289	7.188	6.099	5.903
$O_{\parallel}^{(-2)}$	−5.756	−5.730	−4.808	−4.862
$O_{\perp}^{(-2)}$	−2.142	−2.017	−2.012	−1.832
		$F_{1u}(TO_1)$		
ω (cm^{-1})	183.45i	136.21i	96.39	179.91i
$\bar{Z}^*$	9.113	6.453	3.954	4.455
		Eigendisplacements		
A	+0.0012	+0.0950	+0.0561	+0.1120
B	+0.0978	+0.0298	−0.0337	+0.0002
O_1	−0.1480	−0.0763	−0.0687	−0.0390
$O_{2/3}$	−0.0774	−0.1254	−0.1103	−0.1215
		$F_{1u}(TO_2)$		
ω (cm^{-1})	176.91	181.36	193.26	202.42
$\bar{Z}^*$	1.937	5.344	5.784	3.268
		Eigendisplacements		
A	+0.0547	−0.0922	−0.0228	−0.0823
B	−0.0800	+0.1116	+0.0781	+0.0698
O_1	−0.0715	−0.0189	−0.0353	−0.0039
$O_{2/3}$	−0.0793	−0.0421	−0.1068	−0.0940
		$F_{1u}(TO_3)$		
ω (cm^{-1})	468.91	589.62	503.07	610.29
$\bar{Z}^*$	1.281	4.269	3.777	4.601
		Eigendisplacements		
A	−0.0012	+0.0083	+0.0024	−0.0065
B	+0.0253	+0.0135	+0.0140	−0.0225
O_1	+0.1767	−0.2213	−0.2315	+0.2353
$O_{2/3}$	−0.1212	+0.0801	+0.0653	−0.0454

[a]$BaZrO_3$ has no instabilities at Γ, whereas the TO_1 mode is unstable for $BaTiO_3$, $CaTiO_3$ and $CaZrO_3$.

turns out to be dominated by the Ca displacements (A-type ferroelectricity) as can be seen from the eigendisplacements displayed in Table III and the red color of the corresponding phonon in Fig. 3(b). Despite this important involvement of the A cation in the polar distortion, its Born effective charge is not strongly anomalous. This has to be ascribed to the fact that the polar distortion of Ca is driven by a steric effect. In fact, we already mentioned that $CaTiO_3$ has a tolerance factor less than one. Therefore the small size of the Ca ionic radius allows its distortion in the cubic perovskite structure. Consequently, the involvement of the oxygens in the distortion is inverted with respect to the $BaTiO_3$ case, as the $O_{2/3}$ lying on the plane perpendicular to the direction of the distortion are now more involved than the apical oxygen (see Table III).

TABLE IV. "On-site" force constants (in Ha/$bohr^2$) related to different atoms in the cubic phase of the four bulk compounds. A positive value means that the atomic position is stable against isolated displacement of the considered atom.

Atom	Direction	$BaTiO_3$	$CaTiO_3$	$BaZrO_3$	$CaZrO_3$
A	$xx = yy = zz$	+0.0893	+0.0269	+0.0550	+0.0099
B	$xx = yy = zz$	+0.1635	+0.2236	+0.2198	+0.2510
O	$xx = yy$	+0.0711	+0.0432	+0.0396	+0.0171
	zz	+0.1454	+0.2624	+0.2135	+0.2909

These results can be rationalized by looking at the effect of the substitution of Ba by Ca on the on-site and interatomic force constants. In fact, the "on-site" force constant of Ca as well as the A-A' interaction are significantly smaller than the corresponding ones in $BaTiO_3$, while the "on-site" force constant of Ti is increased. Additionally, the destabilizing A-O_1 interaction (xx', Table V) becomes significantly positive in agreement with the opposite direction of the respective atomic eigendisplacements (Table III), whereas along the Ti-O_1 chain a stronger repulsive interaction prevents an important participation of the B cation to the polar distortion.

These previous observations can be also related to the concurrent appearance of AFD distortions in the system. Although the IFCs between the reported pairs of oxygen are remarkably similar in $BaTiO_3$ and $CaTiO_3$ (and also in $BaZrO_3$ and $CaZrO_3$ as we will see below), the oxygens tilting is favored by the fast decrease of the oxygen "on-site" forces (linked to the destabilizing A-O_1 interaction) in the directions perpendicular to the B-O chains and to the increasing stiffness in the parallel direction (Table IV). Moreover, the phonon dispersion curves appear substantially flat along R-M suggesting the absence of coupling between the oxygens in different planes, but, as can be seen in Tables V and VI, the transverse interactions are far to be negligible. As proposed in Ref. [9], this could be due to the joint action of the A-O coupling with a compensation between different interplane interaction of the oxygens (see also Ref. [41]).

3. $CaZrO_3$

$CaZrO_3$ exhibits much more intricate phonon branches than $CaTiO_3$. However, the dynamical properties of both compounds show some similarities. As in $CaTiO_3$, the strongest instabilities of $CaZrO_3$ are at the R and M points of the Brillouin zone and associated to AFD oxygen rotations ($\omega \simeq 238i$ and $\simeq$233i cm^{-1}, respectively). Also, the dispersion curve along R-M appears completely flat.

Nevertheless, the lowest polar instability is no more confined at Γ, but the polar-antipolar instability extends all over the cubic Brillouin zone. This reflects a FE instability more localized in real space.

In $CaZrO_3$, the distortion is fully driven by the A cation (Ca) and the $O_{2/3}$ anions. In fact, Zr on the B site does not participate to the polar distortion with also subsequent reduced participation of the apical O_1 [see Table III (TO_1 mode)]. Finally, the dynamical effective charges of both Zr and $O_{\parallel}$ appear less anomalous than in the titanates, resulting in a lower value of the mode effective charge.

TABLE V. Interatomic force constants in (Ha/bohr^2) between different pairs of atoms in their local coordinates system, $xx'(\parallel)$, $yy'(\perp)$, and $zz'(\perp)$ for ABO_3 bulk compounds. Transverse ($\perp$) directions for some atomic pairs are degenerate. The two different dipole-dipole (DD) and short-range (SR) contributions also reported.

		$BaTiO_3$			$CaTiO_3$			$BaZrO_3$			$CaZrO_3$		
Atoms		Total	DD	SR	Total	DD	SR	Total	DD	SR	Total	DD	SR
$A-A'$	($\parallel$)	−0.0115	−0.0054	−0.0061	−0.0085	−0.0056	−0.0029	−0.0094	−0.0062	−0.0032	−0.0071	−0.0064	−0.0007
	($\perp$)	+0.0039	+0.0027	+0.0012	+0.0040	+0.00281	+0.0012	+0.0130	+0.0106	+0.0024	+0.0042	+0.0032	+0.0010
$B-B'$	($\parallel$)	−0.0693	−0.0379	−0.0314	−0.0788	−0.0438	−0.0350	−0.0564	−0.0308	−0.0256	−0.0593	−0.0323	−0.0270
	($\perp$)	+0.0078	+0.090	−0.0111	+0.0084	+0.0219	−0.0135	+0.0071	+0.0154	−0.0083	+0.0065	+0.0162	−0.0097
$B-O_1$	($\parallel$)	+0.0037	+0.2394	−0.2357	−0.0382	+0.2794	−0.3176	−0.0409	+0.1940	−0.2349	−0.0719	+0.2129	−0.2847
	($\perp$)	−0.0203	−0.0445	+0.0243	−0.0184	−0.0492	+0.0308	−0.0166	−0.0406	+0.0240	−0.0148	−0.0401	+0.0253
$A-B$	($\parallel$)	−0.0298	−0.0220	−0.0078	−0.0266	−0.0242	−0.0025	−0.0281	−0.0212	−0.0069	−0.0244	−0.0221	−0.0023
	($\perp$)	+0.0139	+0.0110	+0.0029	+0.0150	+0.0121	+0.0029	+0.0130	+0.0106	+0.0024	+0.0133	+0.0111	+0.0023
$A-O_1$	(xx')	−0.0022	+0.0119	−0.0140	+0.0108	+0.0125	−0.0017	+0.0058	+0.0129	−0.0070	+0.0141	+0.0126	+0.0015
	(yy')	−0.0042	−0.0059	+0.0017	−0.0055	−0.0062	+0.0007	−0.0051	−0.0064	+0.0013	−0.0056	−0.0063	+0.0007
	(zz')	−0.0111	−0.0160	+0.0049	−0.0116	−0.0177	+0.0061	−0.0105	−0.0154	+0.0049	−0.0107	−0.0167	+0.0060
O_1-O_4	(xx')	−0.0020	−0.0033	+0.0013	−0.0022	−0.0035	+0.0012	−0.0019	−0.0034	+0.0014	−0.0020	+0.0012	+0.0078
	(yy')	+0.0018	+0.0016	+0.0002	+0.0014	+0.0017	−0.0003	+0.0018	+0.0017	+0.0001	+0.0012	+0.0016	−0.0003
	(zz')	+0.0093	+0.0118	−0.0025	+0.0107	+0.0139	−0.0032	+0.0070	+0.0096	−0.0026	+0.0078	+0.0110	−0.0032
O_1-O_5	(xx')	−0.0004	+0.0016	−0.0020	−0.0009	+0.0017	−0.0026	−0.0009	+0.0017	−0.0026	−0.0013	+0.0016	−0.0028
	(yy')	−0.0004	+0.0016	−0.0020	−0.0009	+0.0017	−0.0026	−0.0009	+0.0017	−0.0026	−0.0013	+0.0016	−0.0028
	(zz')	−0.0339	−0.0236	−0.0102	−0.0379	−0.0278	−0.0101	−0.0345	−0.0191	−0.0154	−0.0372	−0.0219	−0.0153

As before, these dynamical properties can be understood in terms of IFCs. In fact, the "on-site" force associated to Ca and the in-plane "on-site" force of O are drastically reduced while for Zr it is strengthened by making the A cation and the $O_{2/3}$ anions highly unstable and the B cation almost fixed with respect to their high-symmetry positions. Accordingly, the Ca-O_1 interatomic force constants are largely dominated by the dipole-dipole interaction, while the Zr-O_1 interaction is strongly repulsive. The interplay between all these features allows the understanding of the strong A-site driven character of the instabilities. In fact, individual Ca displacements are nearly unstable (Table IV). A proper comparison of $CaZrO_3$ an $CaTiO_3$ with respect to $PbZrO_3$ and $PbTiO_3$, respectively, can be done via the lattice dynamics analysis presented in Ref. [9].

4. $BaZrO_3$

Starting from the analyzed dynamics in $BaTiO_3$ and $CaZrO_3$, the dynamical properties of $BaZrO_3$ are fairly predictable. The substitution of the Ti atoms with Zr on the B-site joined to the presence of Ba on the A site leads to the stability of the cubic phase, also confirmed by steric arguments, since the tolerance factor is close to 1. In fact, unlike the previous perovskite systems, the phonon spectrum of

TABLE VI. Interatomic force constant matrix in (Ha/bohr^2) between other pairs of oxygen in the Cartesian coordinates system. Rows and columns of the matrices correspond, respectively, to x, y, and z directions.

Atoms		
	$BaTiO_3$	$CaTiO_3$
O_1-O_2	$\begin{pmatrix} +0.0038 & 0.0000 & 0.0000 \\ 0.0000 & -0.0091 & +0.0284 \\ 0.0000 & +0.0126 & -0.0091 \end{pmatrix}$	$\begin{pmatrix} +0.0057 & 0.0000 & 0.0000 \\ 0.0000 & -0.0120 & +0.0322 \\ 0.0000 & +0.0177 & -0.0120 \end{pmatrix}$
	$BaZrO_3$	$CaZrO_3$
	$\begin{pmatrix} +0.0039 & 0.0000 & 0.0000 \\ 0.0000 & -0.0060 & +0.0234 \\ 0.0000 & +0.0110 & -0.0060 \end{pmatrix}$	$\begin{pmatrix} +0.0051 & 0.0000 & 0.0000 \\ 0.0000 & -0.0071 & +0.0249 \\ 0.0000 & +0.0137 & -0.0071 \end{pmatrix}$
	$BaTiO_3$	$CaTiO_3$
O_1-O_6	$\begin{pmatrix} -0.0007 & -0.0007 & +0.0013 \\ -0.0013 & +0.0014 & +0.0025 \\ +0.0007 & +0.0007 & +0.0014 \end{pmatrix}$	$\begin{pmatrix} -0.0007 & -0.0006 & +0.0017 \\ -0.0017 & +0.0015 & +0.0029 \\ +0.0006 & +0.0005 & +0.0015 \end{pmatrix}$
	$BaZrO_3$	$CaZrO_3$
	$\begin{pmatrix} -0.0077 & -0.0007 & +0.0013 \\ -0.0013 & +0.0012 & +0.0021 \\ +0.0007 & +0.0006 & +0.0012 \end{pmatrix}$	$\begin{pmatrix} -0.0007 & -0.0005 & +0.0016 \\ -0.0016 & +0.0013 & +0.0023 \\ +0.0005 & +0.0004 & +0.0013 \end{pmatrix}$

$BaZrO_3$ shows only a very weak instability at the R-point with associated phonon frequency $\omega \simeq 60.2i\,\mathrm{cm}^{-1}$ and no unstable polar modes.

By looking at the specific quantities reported in Table III, the softest polar mode (TO_1) displays the smallest polarity ($\bar{Z}^*$) with respect to the corresponding modes in the other compounds. Moreover, unlike Ti in $BaTiO_3$, a tendency of Zr to decrease the spontaneous polarization results from the specific combination of the associated pattern of distortion with the dynamical charges. Conversely, the second stable polar mode (TO_2), even if stiffer, displays bigger polarity because of the additive contribution of Zr and O.

This behavior can be justified by means of the force constants. In fact, the B cation experiences an increased "on-site" term as well as O in its transversal direction with respect to the case of $BaTiO_3$. The Zr-O_1 is strongly dominated by the short-range forces. On the other hand, the A cation shows an "on-site" force constant in between $BaTiO_3$ and $CaTiO_3$, but the A-O interaction is still too weak to destabilize Ba (see Tables IV and V).

For all the four compounds, the interatomic force constants associated to the A-B cations and to the O-O interactions have the same sign and order of magnitude. This trend points out the key role played by the on-site force constants in generating different kinds of instabilities according to the environment that each atom experiences in the different perovskites. In fact, changes in the A-O and B-O interactions (Tables IV and V) are primarily associated to changes of that values.

B. Energetics of metastable phases

In the previous section, we have seen that the parent compounds can develop two types of instability: an FE instability associated to a polar mode at Γ and AFD instabilities associated to unstable modes at M and R. Now we quantify the energy difference associated to the condensation of the corresponding (polar and nonpolar) distortions with respect to the cubic phase. The results are shown in Fig. 4. A careful crystallographic explanation of the symmetry changes associated to these distortions can be found in Ref. [42].

1. $BaTiO_3$

In $BaTiO_3$, the energy sequence of the polar phases arising from the condensation of the polar mode is in line with the experimental sequence of phase transitions when lowering the temperature ($Pm\bar{3}m \rightarrow P4mm \rightarrow Amm2 \rightarrow R3m$). At the same time, we do not find any other distorted structure as a possible metastable phase. To be noticed is that the energy landscape is relatively flat. The $R3m$ ground state is only 20 meV/f.u. below the paraelectric $Pm\bar{3}m$ phase and the energy difference between the polar phases is ≃5 meV/f.u.

2. $CaTiO_3$

Interestingly, in $CaTiO_3$, the energy sequence of the polar phases, arising from the condensation of the unstable polar mode, is reversed. In addition, the relative energy difference is larger than in $BaTiO_3$. In fact, the tetragonal $P4mm$ structure is the lowest-energy configuration among the polar ones with a relative energy gain of about 70 meV/f.u. Moreover, additional nonpolar structures arising from the condensation of the unstable AFD modes at M and R appear as metastable or eventually stable. As usual in perovskites with $t < 1$ [42], in fact, the ground state corresponds to the $Pnma$ ($a^-b^+a^-$) structure, which is ≃−350 meV per f.u. below the reference cubic phase. One-tilt structures, such as $P4/mbm$ ($a^0a^0c^+$) or $I4/mcm$ ($a^0a^0c^-$), and the two-tilts $Imma$ ($a^0b^-b^-$) are intermediate metastable structures that appear ≃100 and ≃50 meV per f.u. above the ground state, respectively.

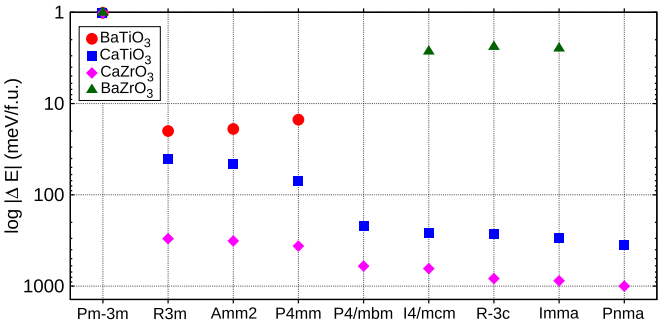

FIG. 4. Energy landscape (in logarithmic scale) for $BaTiO_3$ (red closed circles), $CaTiO_3$ (blue closed squares), $CaZrO_3$ (pink closed rhombus), and $BaZrO_3$ (green closed triangle). For each ABO_3 perovskite, we report the energy gain with respect to the corresponding simple cubic phase, for different optimized phases allowed by dynamical properties (phonon spectra Fig. 3). Polar distortions, characterizing ferroelectric structures, and antiferrodistortive motions, characterizing nonpolar distorted structures, have been taken into account separately. All the structures have been fully relaxed within GGA-WC functional. Main features for the different structures are reported in Table VII.

TABLE VII. Space group and main active modes in the two allowed classes of distortions. By referring to the simple cubic Brillouin zone: polar motion is due to instabilities at Γ (0,0,0), oxygen tilting to instabilities at M ($\frac{1}{2},\frac{1}{2},0$) and R ($\frac{1}{2},\frac{1}{2},\frac{1}{2}$), and antipolar motion to instabilities at X ($\frac{1}{2}$,0,0), or to the trilinear coupling with the two latter instabilities [42,43], as in $CaTiO_3$. The polarization direction associated to the ferroelectric structures and Glazer notation associated to the antiferrodistortive structures are also reported.

Space group	Notation	Modes
	Polar structures	
$P4mm$ (99)	$a_0a_0a_1$	Γ_4^-
$Amm2$ (38)	$a_0a_1a_1$	Γ_4^-
$R3m$ (160)	$a_1a_1a_1$	Γ_4^-
	Antiferrodistortive structures	
$P4/mbm$ (127)	$a^0a^0c^+$	M_3^+
$I4/mcm$ (140)	$a^0a^0c^-$	R_4^+
$Imma$ (74)	$a^0b^-b^-$	R_4^+
$R\bar{3}c$ (167)	$a^-a^-a^-$	R_4^+
$Pnma$ (62)	$a^-b^+a^-$	R_4^+, M_3^+, X_5^+

TABLE VIII. Overlap matrix between the total distorsion $\boldsymbol{\tau}$ of the three optimized polar structures and the eigendisplacements $\boldsymbol{\eta}_i$ associated to the F_{1u}(TO) modes of the optimized cubic phase, $\langle \boldsymbol{\eta}_i | M | \boldsymbol{\tau} \rangle = \alpha_i$. The distortion $\boldsymbol{\tau}$ has been normalized such that $\langle \boldsymbol{\tau} | M | \boldsymbol{\tau} \rangle = 1$, with M in atomic mass units, and results to be defined as $\boldsymbol{\tau} = \sum_{i=1,2,3} \alpha_i \boldsymbol{\eta}_i$, with $|\boldsymbol{\tau}| = \sqrt{\langle \boldsymbol{\tau} | M | \boldsymbol{\tau} \rangle}$. Since $BaZrO_3$ has no polar instabilities, we reported results only for $BaTiO_3$, $CaTiO_3$, and $CaZrO_3$.

	$P4mm$	$Amm2$	$R3m$
	$BaTiO_3$		
$\lvert\boldsymbol{\tau}\rvert$	0.188	0.209	0.214
$F_{1u}(TO_1)$	0.993	0.975	0.971
$F_{1u}(TO_2)$	0.110	0.087	0.129
$F_{1u}(TO_3)$	0.032	0.194	0.228
	$CaTiO_3$		
$\lvert\boldsymbol{\tau}\rvert$	0.601	0.478	0.435
$F_{1u}(TO_1)$	0.985	0.970	0.970
$F_{1u}(TO_2)$	−0.171	−0.203	−0.199
$F_{1u}(TO_3)$	0.033	0.129	−0.143
	$CaZrO_3$		
$\lvert\boldsymbol{\tau}\rvert$	0.903	0.886	0.868
$F_{1u}(TO_1)$	0.976	0.910	0.897
$F_{1u}(TO_2)$	−0.060	0.202	−0.208
$F_{1u}(TO_3)$	−0.067	−0.336	−0.197

3. $CaZrO_3$

In $CaZrO_3$, the energy sequence of both the polar and AFD phases is the same as $CaTiO_3$, but they are shifted down in energy becoming very spread. The AFD $Pnma$ ground-state is lower by about −1 eV/f.u. than the $Pm\bar{3}m$ phase. This is in tune with the very high transition temperature experimentally observed for the sequence $Pm\bar{3}m \rightarrow Pnma$, even if the phonon frequencies related to the unstable modes are close to the ones in $CaTiO_3$.

4. $BaZrO_3$

For $BaZrO_3$, we found competitive $R\bar{3}c$ ($a^-a^-a^-$), $Imma$ ($a^0b^-b^-$), and $I4/mcm$ ($a^0a^0c^-$) antiferroditortive structures. According to the very tiny value of the instability [Fig. 3(c)], the condensation of the oxygen rotations provides an energy gain relative to the cubic phase of about ≃2.5 meV per f.u., while the three distorted phases have an energy that differs by less than 0.2 meV/f.u. In spite of the negligible energy gain, the amplitude of the AFD distortion is significant. The biggest distortion is appearing in the tetragonal phase with an angle of rotation of ∼4° about the [001] direction.

5. *Polar modes and ferroelectric phases*

In order to interlock the optimized polar structures with the lattice dynamics, we evaluated the contribution of each polar mode to the condensed distortion. The overlap matrix is reported in Table VIII. It is interesting to notice that the three ferroelectric states are mostly due to the condensation of the unstable optical mode for all the three perovskites $BaTiO_3$, $CaTiO_3$, and $CaZrO_3$, so that it is possible to establish a nearly one-to-one correspondence with the pattern of distortion associated to the unstable TO_1 mode and the displacements as obtained from the structural optimization, while the contribution of the TO_2 and TO_3 modes remains very small.

An important remark is the huge difference in the total distortion $\boldsymbol{\tau}$ between $BaTiO_3$ and the Ca-based perovskites, which allows for possible bigger spontaneous polarization in the latter compounds even if the A cation at play is not either stereochemically active or involved in the hybridization with the oxygens, like Ti in $BaTiO_3$.

The previous analysis of the dynamics and energetics associated to the four parent compounds has emphasized some similarities and differences. This is helpful for a better understanding of properties arising while mixing cations at the A and B sites in $(Ba,Ca)TiO_3$ and $Ba(Ti,Zr)O_3$ solid solutions, respectively. We will now present results coming from a systematic characterization of the latter systems by also testing and comparing two different approaches: the "virtual crystal approximation" (VCA) and supercell-based calculations.

We note that the parent $BaTiO_3$ and $CaTiO_3$ compounds display inverted sequence of polar phases. Then, for the $(Ba,Ca)TiO_3$ solid solutions, the emergence of a region with strong competition between these phases and a crossing point in energetics can be expected. This will be confirmed in the next section.

IV. $(Ba,Ca)TiO_3$ SOLID SOLUTIONS

In the last few years, $Ba_{1-x}Ca_xTiO_3$ (BCT) has started to arouse curiosity in the experimental community as the Ca off-centering seems to play an important role in stabilizing ferroelectricity against chemical pressure effects [44–46]. In particular, in Ref. [45], Fu and Itoh have characterized single crystals of BCT in a temperature range from 2 to 400 K and for compositions ranging from $x = 0.00$ up to $x = 0.34$. They found that the Curie point is nearly independent of the Ca concentration for the $Pm\bar{3}m \rightarrow P4mm$ transition, whereas there is a shift of the $P4mm \rightarrow Amm2$ and $Amm2 \rightarrow R3m$ phase transitions toward lower temperatures. Accordingly, the consequence of Ca substitution is the stabilization of the tetragonal ferroelectric phase.

Let us now analyze the dynamics and energetics as predicted by means of first-principles calculations. We first report results from the VCA approach in Sec. IV A, then from the use of supercells in Sec. IV B.

A. VCA approach

1. *Lattice parameter*

First, we report the evolution of the lattice parameter of the $Pm\bar{3}m$-cubic phase as obtained from the structural optimization within VCA. Because of the reduced volume of $CaTiO_3$ with respect to $BaTiO_3$ (Table I), the lattice parameter decreases monotonically with the Ca concentration, but the trend deviates from the linearity of the Vegard's law, as shown in Fig. 5(a).

As for the pure compounds, for solid solutions we can define the tolerance factor as $t = (\overline{r_A} + r_O)/\sqrt{2}(r_B + r_O)$, with $\overline{r_A} = (1-x)r_{Ba} + (x)r_{Ca}$. Values of the ionic radii, r_i, for the pure atoms have been taken from Ref. [47]. For increasing x, t

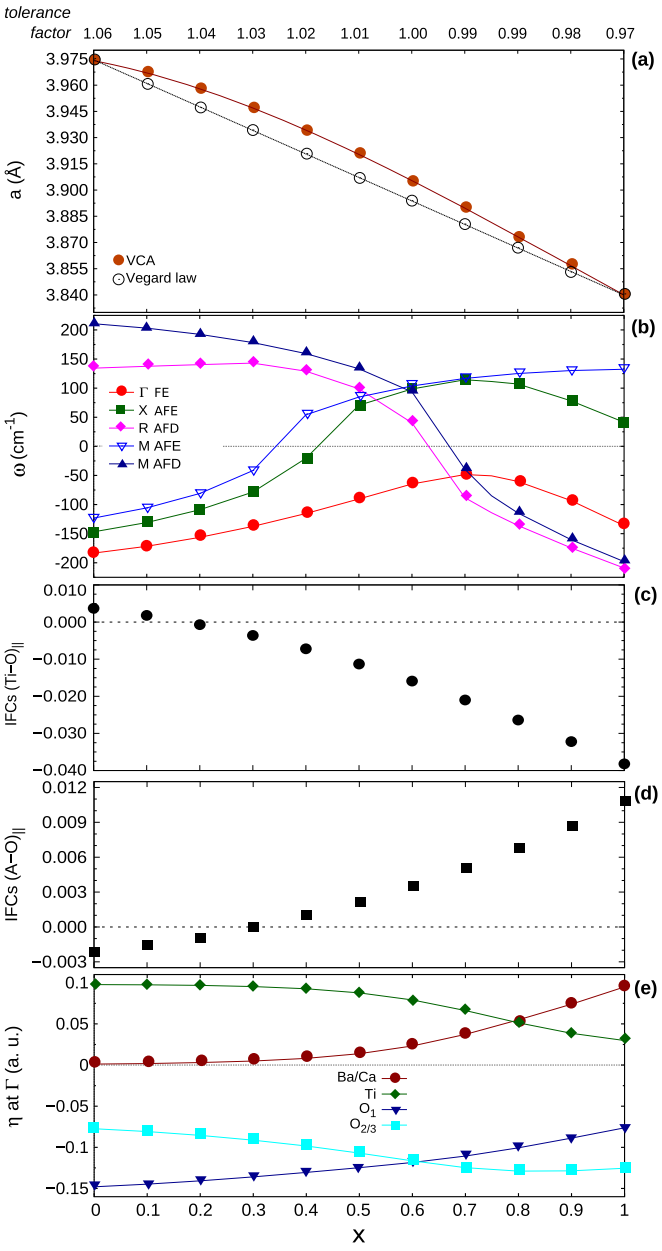

FIG. 5. Evolution of different lattice properties as a function of x composition in $Ba_{1-x}Ca_xTiO_3$ as obtained by the use of VCA. (a) Cubic lattice parameter a_{cell} (in angstrom). Vegard's law has been built on the theoretical values of the cubic $BaTiO_3$ and $CaTiO_3$ reported in Table I: $a(x) = (1-x)a_{BTO} + (x)a_{CTO}$. (b) Trend of the lowest phonon frequencies at the high-symmetry points of the simple cubic Brillouin zone. Evolution of the total Ti-O (c) and A-O (d) interatomic force constants (IFCs in Ha/bohr^2). (e) Evolution of normalized eigendisplacements (in a.u.) associated to the unstable polar mode at the Γ point of the simple cubic Brillouin zone. Lines are guide for the eyes.

decreases from 1.06 to 0.97 reaching 1 at $x = 0.6$, as reported on top of Fig. 5.

2. *Dynamical properties*

Then, we analyze the evolution of the lowest phonon frequencies at the high symmetry points of the Brillouin zone of the cubic reference. DFPT calculations have been performed on the optimized structures. We find that, for increasing Ca-concentration, the original polar instabilities of $BaTiO_3$ changes character by becoming confined to the center of the Brillouin zone (AFE instabilities at X and M disappear), while the AFD modes become unstable, as shown Fig. 5(b). Changes in the phonon instabilities are linked to the evolution of t. In fact, the polar instability dominates until t becomes smaller than one at which the AFD modes become largely unstable. Specifically, the lattice dynamics is $BaTiO_3$-like for $0 \leqslant x \leqslant 0.2$. The unstable polar mode at Γ is mainly sustained by the destabilizing Ti-O interaction, while the A-O interaction stays mostly repulsive, resulting in the inactivity of the A site, as reproduced in Figs. 5(c)–5(e). Accordingly, the instabilities at the X and M points are also due to Ti-O polar motion. For $0.3 \leqslant x \leqslant 0.6$, the scenario starts to change. The polar instability becomes weaker as it results from the important reduction in the amplitude of the associated frequencies. Particularly, the polar distortion remains unstable at Γ, while it becomes progressively stable at X and M. These smooth changes can be related to smooth changes in the type of interaction between the cations and the oxygens. A change of sign is observed along both the Ti-O and A-O interactions that corresponds to a strong competition between attractive and repulsive forces in determining the nature and character of the polar instability: a reduction of the amplitude of the Ti-motion corresponds to increasing negative value of the Ti-O interaction, while an increasing contribution to the polar distortion of the A-site arises from positive values of the A-O interaction, as shown in Figs. 5(c)–5(e). Finally, for $0.7 \leqslant x \leqslant 1.0$, the lattice dynamics becomes $CaTiO_3$-like. Accordingly, instabilities related to oxygen rotations appear at the M and R points of the cubic Brillouin zone and are more unstable than the polar one at Γ. This situation results from strong destabilizing A-O interactions and largely repulsive Ti-O interactions. Accordingly, the character of the polar distortion also changes by becoming largely driven by the motion of the A site with respect to the B one.

Moreover, changes in the phonon behavior also affect the dynamics of the oxygens. The increasing contribution to the distortion from the A site, i.e., increasing long-range forces between the A cation and oxygens, favors the motion of the planar oxygens with respect to the apical one [labelled $O_{2/3}$ and O_1 in Fig. 5(e), respectively]. Specifically, the contribution is reversed when going from $t > 1$ to $t < 1$.

The latter analysis of the evolution of the dynamical properties when going from the $BaTiO_3$-rich region to the $CaTiO_3$-rich one in the $Ba_{1-x}Ca_xTiO_3$ "virtual-system" reveals the presence of two parallel mechanisms: the progressive weakening of the long-range forces between Ti and O atoms in favor of their strengthening between the A atoms and oxygens. In terms of character of the phonons instabilities, this change corresponds to a smooth evolution from the B-driven into the A-driven distortions associated to the parents $BaTiO_3$ and $CaTiO_3$, respectively. The reasons behind these two phenomena are also different and complementary. In fact, Ca doping of the virtual A-site produces: (i) varying interatomic force constants between the A-O atomic pair in favors of destabilizing long-range forces sustained by the progressive lowering of the A-cation stiffness when going

TABLE IX. Interatomic force constants for $Ba_{0.875}Ca_{0.125}TiO_3$ from VCA and supercell calculations. Units are in Ha/bohr^2. Directions $xx'(\|)$, $yy'(\perp)$, and $zz'(\perp)$ refer to local coordinates system of the different pairs of atoms. Distances (in angstrom) between the selected atoms are also reported. Atoms' notation in the second column is consistent with Fig. 8(a).

$Ba_{0.875}Ca_{0.125}TiO_3$									
VCA					$2 \times 2 \times 2$ cell				
Atoms		Total	DD	SR	Atoms		Total	DD	SR
A-A'					Ba-Ba′	($\|$)	−0.012	−0.006	−0.006
$d = 3.967$ Å	($\|$)	−0.011	−0.005	−0.006	$d = 3.959$ Å	($\perp$)	+0.004	+0.003	+0.001
	($\perp$)	+0.004	+0.003	+0.001	Ca-Ba	($\|$)	−0.009	−0.005	−0.004
					$d = 3.959$ Å	($\perp$)	+0.004	+0.003	+0.001
B-B'	($\|$)	−0.070	−0.038	−0.032	Ti-Ti′	(xx')	−0.072	−0.040	−0.033
$d = 3.967$ Å	($\perp$)	+0.008	+0.019	−0.011	$d = 3.929$ Å	(yy')	+0.008	+0.020	−0.012
						(zz')	+0.009	+0.020	−0.011
A-B					Ba-Ti	($\|$)	−0.030	−0.022	−0.008
$d = 3.436$ Å	($\|$)	−0.030	−0.022	−0.008	$d = 3.437$ Å	($\perp$)	+0.014	+0.011	+0.003
	($\perp$)	+0.014	+0.011	+0.003	Ca-Ti	($\|$)	−0.023	−0.022	−0.001
					$d = 3.403$ Å	($\perp$)	+0.013	+0.011	+0.003
B-O_1					Ti-O_1	($\|$)	+0.005	+0.236	−0.231
$d = 1.984$ Å	($\|$)	+0.002	+0.242	−0.241	$d = 1.994$ Å	($\perp$)	−0.020	−0.045	+0.025
	($\perp$)	−0.020	−0.045	+0.025	Ti-O_2	($\|$)	−0.007	+0.253	−0.260
					$d = 1.965$ Å	($\perp$)	−0.020	−0.044	+0.024
A-O_1					Ba′-O_1	(xx')	−0.004	+0.012	−0.016
$d = 2.805$ Å					$d = 2.783$ Å	(yy')	−0.011	−0.016	+0.005
						(zz')	−0.004	−0.006	+0.002
	(xx')	−0.001	+0.012	−0.013	Ba′-O_2	(xx')	−0.003	+0.012	−0.015
	(yy')	−0.004	−0.006	+0.002	d=2.800 Å	(yy')	−0.005	−0.006	+0.001
	(zz')	−0.011	−0.016	+0.005		(zz')	−0.011	−0.016	+0.005
					Ca-O_2	(xx')	+0.011	+0.011	−0.000
					$d = 2.750$ Å	(yy')	−0.005	−0.006	+0.001
						(zz')	−0.011	−0.016	+0.005

from $BaTiO_3$ to $CaTiO_3$ (see Table IV); (ii) reduction of the volume, that can be considered as increasing isotropic pressure on the $ATiO_3$ system and, therefore, shortening of the Ti-O bond lengths. The latter effect produces increasing stiffness of Ti atoms, that results in the change of sign of the Ti-O interatomic force constants and associated weakening of the B-type ferroelectricity. In fact, as investigated at the first-principles level in Refs. [48–50] and as it turns out when comparing graphs (a) and (c) reported in Fig. 5, the balance between short-range and long-range forces between the Ti and O atoms is strongly sensitive to pressure. At variant, the varying composition does not affect significantly the A-B interaction, which in fact remains almost the same as in the pure parent compounds (see Tables V and IX).

3. *Energy landscape*

As we previously did for the pure parent compounds, now that the main instabilities of BCT "virtual system" have been identified, we look at the energy competition between different phases arising from the condensation of the corresponding modes in order to obtain an overview of the energetics as a function of concentration. As shown in Fig. 6, the main effect of the Ca substitution is to reduce the energy gain both between the three ferroelectric phases and with respect to the cubic phase by making them strongly competitive, while additional antiferrodistortive structures appear as metastable in the $CaTiO_3$-rich region by providing a nonpolar ground-state.

Such behavior proceeds from the evolution of the dynamical properties previously analyzed. In fact, an important energy

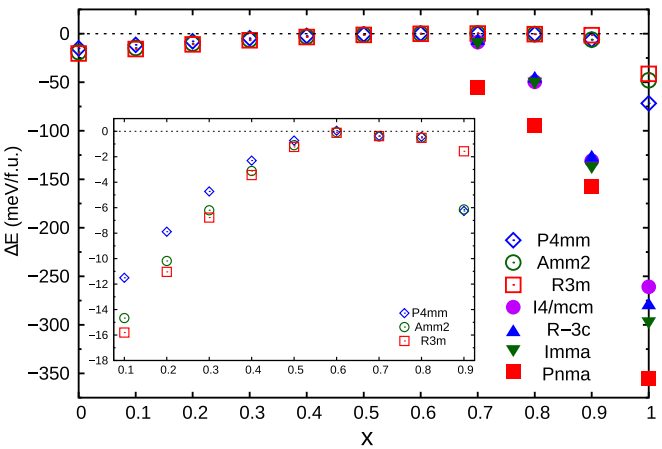

FIG. 6. Energy gain with respect to the simple cubic phase for different optimized structures allowed by dynamical properties within VCA as a function of x composition in $Ba_{1-x}Ca_xTiO_3$. Structures properties reported in Table VII. The inset shows a zoom on the energetics of the polar phases for $0.1 \leqslant x \leqslant 0.9$.

competition between polar phases starts at $x = 0.3$, that corresponds to the concentration where we observe the change of sign of the Ti-O IFCs [see Fig. 6(c)]. Then, the energies of the polar phases smoothly converge to that of the cubic one in line with the progressive weakening of the polar instability. Noteworthy is that the inversion in the energy sequence of the three polar phases happens at $x = 0.9$ where we observe the inversion of the dominant character of the polar instability between virtual A cation and Ti [see Fig. 6(e)].

Additional structures with oxygen rotations appear with a higher energy gain from $x = 0.7$ proceeding from the appearance of the AFD phonons instabilities [see Figs. 5(b) and 6]. It is also noteworthy that the contribution to the polar distortion arising from the apical and planar oxygens is inverted from this point, with the dominant motions of the latter ones [see Fig. 5(e)].

4. Polarization and piezoelectric response

Proceeding from the previous observation that for $0.0 \leqslant x \leqslant 0.6$ the BCT "virtual-system" experiences a progressive weakening of the ferroelectric instability and that no other phonons are unstable, we now evaluate the evolution of the spontaneous, P_s, and piezoelectric coefficients, d_{ij}. According to the VCA results, we performed calculations on the lowest energy rhombohedral $R3m$ structure (Fig 6). Values are normalized to the calculated ones of pure $R3m$-$BaTiO_3$, which are $P_s^{\mathrm{BTO}} \simeq 38\ \mu\mathrm{C/cm}^2$ and $d_{11}^{\mathrm{BTO}} \simeq 76$ pC/N, and $d_{15}^{\mathrm{BTO}} \simeq 270$ pC/N and $d_{33}^{\mathrm{BTO}} \simeq 15$ pC/N.

Specifically, in Fig. 7, we report P_s as obtained both via first-principles calculations by means of the Berry phase theory [51] (blue circles) and via the Born effective charges by means of the approximation $P_{s,\alpha} = \frac{1}{\Omega}\sum_{k,\beta} Z^*_{k,\alpha\beta}\Delta\tau_{k,\beta}$ [52] (green rhombus). It results that P_s decreases as a function of increasing Ca composition in tune with the decreasing energy gain associated to the polar phases in this range of composition, i.e., the weakening of the polar instability detected within VCA (Figs. 5 and 6). In order to clarify if changes in the polarization are mostly due to varying effective charges or atomic distortions, we disentangled the two contributions. In the first case, we kept constant the atomic displacements of pure $R3m$ $BaTiO_3$ and took into account the different effective charges associated to each BCT compositions (orange triangles). In the second case, we kept constant the Born effective charges of pure $R3m$ $BaTiO_3$ and considered the distortion arising from different compositions (red circles). It results in that the evolution of P_s has to be widely ascribed to changes in atomic distortion in BCT "virtual system" in such range of composition, as shown in Fig. 7 (top). In fact, this behavior is in line with the evolution of the eigendisplacements associated to the unstable polar mode at Γ with a pronounced reduction of the titanium and oxygens motion Fig. 5(e).

Despite the decrease of polarization, the piezoelectric response increases with the Ca-concentration (Fig. 7 bottom). This trend is due to the fact that the stress-free dielectric response, ε_{ij}, remarkably increases as well, as shown in the inset of Fig. 7. By writing down the piezoelectric coefficient as $d_{ik} = \frac{de_{s,i}}{dE_k} \propto (\chi_{j,k}P_{s,l} + P_{s,j}\chi_{l,k})$ [53], it is easier to understand such behavior: near a phase transition, where the lowest-frequency polar mode, i.e., the soft mode, goes to zero, the dielectric response diverges [54]. Accordingly, the calculated values of the lowest-frequency polar modes in the $R3m$ phase evolve like 169, 160, 124, 73 (in cm^{-1}) for 0.0, 0.2, 0.4, and 0.6 x composition, respectively. Therefore the softening of the polar mode overcomes the reduction of P_s in the piezoelectric response within the VCA approach.

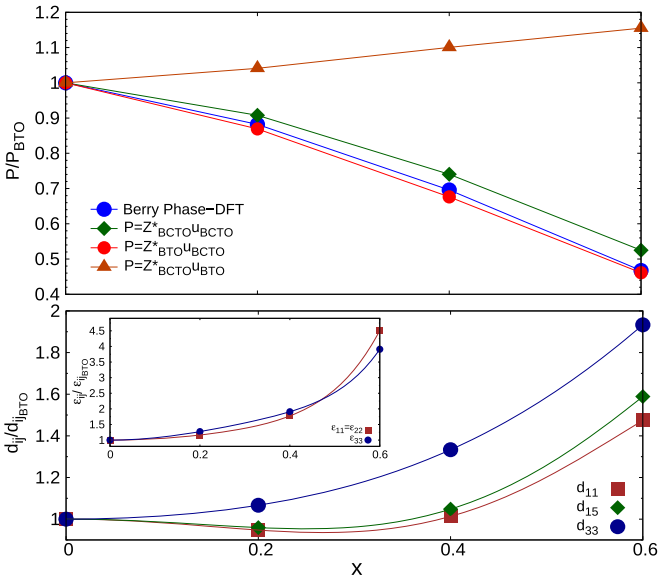

FIG. 7. Evolution of polarization, piezoelectric and stress-free dielectric coefficients in the rhombohedral-$R3m$ phase as a function of x composition in $Ba_{1-x}Ca_xTiO_3$ within VCA. Values are normalized to the ones of $R3m$ $BaTiO_3$: $P_s^{\mathrm{BTO}} \simeq 38\ \mu\mathrm{C/cm}^2$; $d_{11}^{\mathrm{BTO}} \simeq 76$ pC/N, $d_{15}^{\mathrm{BTO}} \simeq 270$ pC/N, and $d_{33}^{\mathrm{BTO}} \simeq 15$ pC/N; $\varepsilon_{11}^{\mathrm{BTO}} \simeq 208$ and $\varepsilon_{33}^{\mathrm{BTO}} \simeq 11$. (Top) Variation of the polarization as directly computed by Berry-phase calculations (blue circles) and by Born effective charges approximation to disentangle the contribution of varying atomic charges and displacements. (Lower) Trend of the d_{ij} coefficient and stress-free dielectric response ε_{ij}.

B. Supercell approach

In order to check the validity of VCA and to better characterize the impact of the (Ba,Ca) substitution on the dynamics of the system, we performed direct DFT calculations on the $Ba_{0.875}Ca_{0.125}TiO_3$ and $Ba_{0.50}Ca_{0.50}TiO_3$ compositions by means of supercells. Details about the atomic arrangements have been provided in Sec. II C.

1. $Ba_{0.875}Ca_{0.125}TiO_3$

Phonons calculations performed at the Γ point of the cubic $Pm\bar{3}m$ supercell of $Ba_{0.875}Ca_{0.125}TiO_3$ [Fig. 2(a)] have revealed several instabilities related to polar modes. The most unstable one, with $\omega \simeq 169\mathrm{i}\ \mathrm{cm}^{-1}$, is associated to a polar distortion driven by all the Ti atoms and the single Ca atom against the oxygens. Ba atoms are almost fixed as in the parent $BaTiO_3$. Therefore Ca is polar active on the A site already at low concentration. The different dynamics can be analyzed in terms of interatomic force constants between the A cations and oxygens in the investigated solid solution. In fact, the A-O interaction results to be opposite if we focus on Ba or Ca atoms in line with the dynamical properties of the respective

pure compounds (Table V). As reported in Table IX, the Ba-O interaction remains dominated by repulsive forces, while the Ca-O interaction is largely dominated by the destabilizing long-range interaction. Moreover, by looking at the atomic pair properties reported in Table IX, a further effect of the Ca-presence is to make oxygens inequivalent even in the high centrosymmetric reference. This effect is due to structural relaxation around the Ca atom because of its smaller size than Ba. This mechanism strongly affects the Ti-O interaction. In fact, the Ti atom experiences shorter and longer bonds with the corresponding apical oxygen that produce strong competition between long- and short-range forces: along the longer bond, the dipole-dipole interaction overcomes the repulsion, while it is the opposite along the shorter bond (see values for the supercell case in Table IX). For this specific $BaTiO_3$-rich concentration, such delicate balance between the attractive and repulsive interactions along the Ti-O bond results in the weakening of the B-site driven ferroelectricity.

The intriguing manifestation of this phenomenon is the achievement of a quasi-degeneracy between different polar states. In fact, we analyzed five different polar states corresponding to the tetragonal, orthorhombic, rhombohedral, monoclinic, and triclinic phases with $P4mm$, $Amm2$, $R3m$, Pm, and $P1$ space-group symmetry, respectively. Specifically, the average gain in energy with respect to the $Pm\bar{3}m$ cubic phase is about -20 meV/f.u. as for the parent $BaTiO_3$. Nevertheless, the maximum energy difference between the different polar phases is of about 0.5 meV/f.u.

According to the latter isotropic energy landscape, the spontaneous polarization results to be essentially the same for all these ferroelectric phases, that is $P_s \simeq 39.5$ μC/cm^2 as obtained via Berry phase calculations. This value is slightly higher than P_s of pure $BaTiO_3$ in the $R3m$ phase showed in Fig. 7 of the previous section. Moreover, we also calculated the d_{ij} coefficients of the piezoelectric tensor in the stable $R3m$ phase. The d_{33} component, parallel to the polarization direction, remains unchanged with respect to $BaTiO_3$, while the d_{11} and d_{15} components, transversal to the polar axis, are considerably enhanced. Specifically, they are $d_{33} \simeq 15$, $d_{11} \simeq 344$, and $d_{15} \simeq 1458$ in pC/N. This behavior can be related to the increase of the stress-free dielectric response along the corresponding directions due to the softening of the polar modes. In fact, the lowest-frequency polar mode in the stable $R3m$ phase is of about 61 cm^{-1} instead of 169 cm^{-1} in $BaTiO_3$.

2. $Ba_{0.5}Ca_{0.5}TiO_3$

First result in $Ba_{0.5}Ca_{0.5}TiO_3$ [Figs. 2(b)–2(d)] is the preference of an ordered configuration composed by alternating layers of the same type of A cations with respect to a columnar and rocksalt ordering. The relative energy gain of the high-symmetry columnar and layered configurations with respect to the rocksalt one is about -35.5 and -81.4 meV/f.u., respectively.

Then, as previously, we performed DFPT calculations on the three high-symmetry reference supercells. All three configurations display several instabilities. In all of them the most unstable mode corresponds to a polar distortion driven by both the Ti and Ca atoms like in $Ba_{0.875}Ca_{0.125}TiO_3$, but

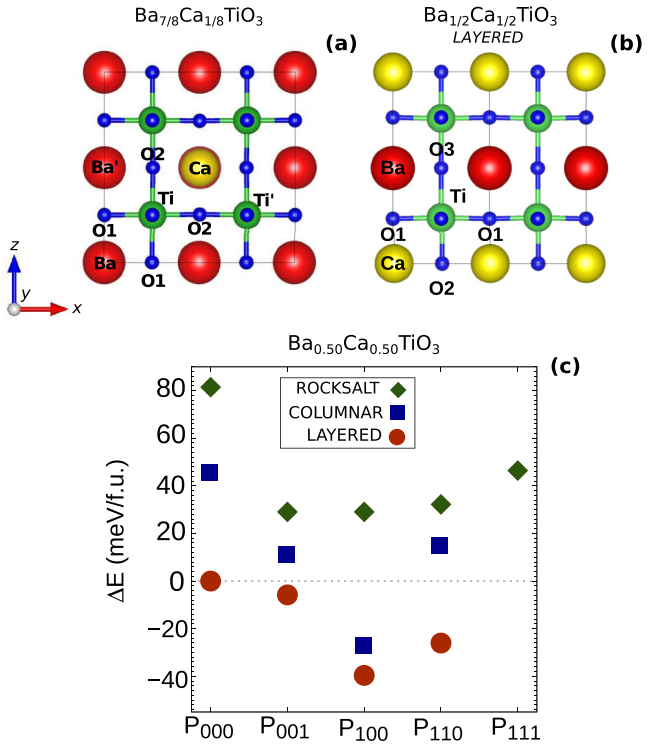

FIG. 8. Schematic representation of the atomic arrangement in $Ba_{0.875}Ca_{0.125}TiO_3$ (a) and in layered $Ba_{0.5}Ca_{0.5}TiO_3$ (b). Direction along y is equivalent to the x one. Labels help the visualization of the main atomic pair analyzed in Tables IX and X. (c) Energy gain (in meV/f.u.) with respect to the high-symmetry $P4mmm$ layered structure for different optimized polar states in the $Ba_{0.5}Ca_{0.5}TiO_3$ supercells. The x-axis notation refers to the direction of the components of polarization.

with an average major contribution from calcium. The phonon frequency associated to that mode is $\omega \simeq 141$i cm^{-1} in all three cases. Additionally, AFD modes related to oxygens rotation become unstable. However, the energy gain carried to the system by the condensation of the latter distortions alone is lower than the one coming from the polar distortions, that determine the ground-state.

Accordingly, the most stable polar phase results to be the $P2mm$ structure with the polarization along the [100] direction of the layered atomic arrangement. The associated P_s is of about 51 μC/cm^2 and it is considerably greater than the one calculated in $P4mm$-$BaTiO_3$, that is $P_s \simeq 34$ μC/cm^2. Moreover, in order to see eventual effects of the atomic configuration on the energy competition between different polar states, we condensed different patterns of polar distortions in the three arrangements. The associated energy landscape is quite spread as reported in Fig. 8(c). The result is that, for $x = 0.50$, the system prefers a state with only "one-component" polarization independently of the atomic configuration. The $R3m$-like state with polarization along the [111] pseudocubic direction is largely penalized.

Also in this case, changes in the dynamical properties (i.e., substantial contribution from Ca atoms to the polar distortion and the appearance of unstable AFD modes) and in the energetics of the polar phases can be analyzed in term of

TABLE X. Interatomic force constants for $Ba_{0.50}Ca_{0.50}TiO_3$ within VCA and the layered supercell. Units are in Ha/bohr^2. Directions $xx'(\parallel)$, $yy'(\perp)$, and $zz'(\perp)$ refer to local coordinates system of the different pairs of atoms. Distances (in angstrom) between the selected atoms are also reported. Atoms' notation in the second column is consistent with Fig. 8(b).

$Ba_{0.50}Ca_{0.50}TiO_3$					
VCA			1 × 1 × 2 cell		
Atoms		Total	Atoms		Total
B-O_1			Ti-O_1	($\parallel$)	−0.009
d = 1.960 Å			d = 1.956 Å	($\perp$)	−0.019
	($\parallel$)	−0.011	Ti-O_2	($\parallel$)	−0.047
	($\perp$)	−0.020	d = 1.890 Å	($\perp$)	−0.017
			Ti-O_3	($\parallel$)	+0.010
			d = 2.011 Å	($\perp$)	−0.019
A-O_1			Ba-O_1	(xx')	−0.001
d = 2.772 Å			d = 2.837 Å	(yy')	−0.005
				(zz')	−0.011
			Ba-O_3	(xx')	−0.005
	(xx')	+0.002	d = 2.765 Å	(yy')	−0.005
	(yy')	−0.005		(zz')	−0.011
	(zz')	−0.011	Ca-O_1	(xx')	+0.010
			d = 2.690 Å	(yy')	−0.006
				(zz')	−0.012
			Ca-O_2	(xx')	+0.011
			d = 2.765 Å	(yy')	−0.005
				(zz')	−0.012

interatomic force constants. As made clear in Tables IX and X, the main features are the same as the ones described for the x = 0.125 Ca concentration. However, the higher concentration of calcium induces shorter Ti-O distances, i.e., more contracted [TiO_6] octahedra. On the one hand, this produces the overall weakening of the long-range interaction between Ti and O atoms in favor of repulsive forces hindering the B-driven polar distortion. Therefore the polar instability remains mostly Ca-driven, promoting "tetragonal-like" polar states. On the other hand, the stiffness of oxygens is reduced in the direction perpendicular to the Ti-O bonds favoring the appearance of oxygen rotations. In fact, the values of the "on-site" oxygens force constants in the solid solution are in between the ones of pure $BaTiO_3$ and $CaTiO_3$ (Table IV).

C. VCA versus supercell approaches

By comparing results from supercell-based calculations with the ones from VCA, it seems that the latter approach is successful to provide an average and qualitative identification of the main changes occurring in the (Ba,Ca)TiO_3 solid solutions. However, it cannot provide a proper description of the microscopic mechanism behind properties. The reason of such a limitation is that, by construction, VCA considers all A atoms as equivalent and forces them to behave similarly while, in fact, Ba and Ca want to adopt different behaviors. The importance of considering the actual local cations is clear by comparing the quantities reported in Tables IX and X, where we clearly see different results are obtained depending on the method. In fact, as discussed above, evolutions in the dynamics as well as in the energy landscape are strongly related to the presence of calcium that directly interacts with the oxygens and, indirectly, affects the Ti-O interaction via local changes of the structure. These effects have a purely steric nature related to the presence of Ca atoms. Strong changes in the dynamical properties as steric effects induced by the addition of Ca have also been found in (Ba,Ca)ZrO_3 [55].

However, the progressive weakening of ferroelectricity, within VCA, is not representative of the real behavior: the actual weakening of the Ti-driven ferroelectricity due to decreasing volume is progressively compensated by the Ca-driven ferroelectricity. In fact, the inversion in the sequence of polar phases when going from $BaTiO_3$ to $CaTiO_3$ appears already at $x = 0.50$ within the supercell, while it is expected for $x \geqslant 0.9$ within VCA. Additionally, an opposite trend of the spontaneous polarization is also obtained within the two approaches: decreasing values for larger x within VCA, while increasing ones within the supercells.

As a global result, the partial success of VCA in detecting changes in the dynamical properties when progressively substituting Ba by Ca is due to two main factors: (i) the volume contraction induced by increasing Ca concentration allows to detect the weakening of the B-driven ferrolectricity and (ii) possible inaccuracies in reproducing the orbital hybridization within VCA are not primary here, as the most relevant hybridization mechanism is only related to the O p and Ti d states, that are not concerned by the VCA mixing procedure. Nevertheless, the trends and microscopic mechanisms involved as predicted by means of supercell calculations are better in line with experimental observations [45,56]. This remark confirms that, in order to provide a proper first-principles characterization of (Ba,Ca)TiO_3, VCA-based approaches can provide some trend, but are not appropriate to explain the underlying physics; for the latter, supercell-based calculations taking explicitly into account the different nature of the cations are more suitable.

V. Ba(Ti,Zr)O_3 SOLID SOLUTIONS

Ba(Ti,Zr)O_3 (BTZ) solid solutions involve the homovalent substitution between Ti^{4+} and Zr^{4+}, which are nevertheless quite different atoms both for the ionic radii (0.605 and 0.72 Å, respectively [47]) and the electronic configuration (Ti $4s^2\,3d^2$ and Zr $4d^2\,5s^2$) entering the hybridization mechanism, which for instance leads the ferroelectricity in $BaTiO_3$. The first experimental investigation of the phase diagram of the $BaTiO_3$-$BaZrO_3$ binary system dates back to the 1956 with the work of Kell and Hellicar [2], reporting the abrupt effect of Zr concentration on the decreasing of the Curie point for the three ferroelectric phases of $BaTiO_3$. Subsequently, other solid experimental investigations came out in the late '90s, when Ravez *et al.* in Refs. [57,58] provided a clear distinction of phases in the $BaTi_{1-y}Zr_yO_3$ ceramics diagram: classical ferroelectric $BaTiO_3$-like for $0.00 \leqslant y \leqslant 0.10$, only one ferroelectric-paralectric transition observed in the range $0.10 \leqslant y \leqslant 0.27$ and relaxor ferroelectric behavior for $0.27 < y \leqslant 0.42$. Then, in 2004, Simon *et al.* also investigated the crossover from a ferroelectric to a relaxor state in lead-free solid solutions in Ref. [59], confirming that beyond a definite

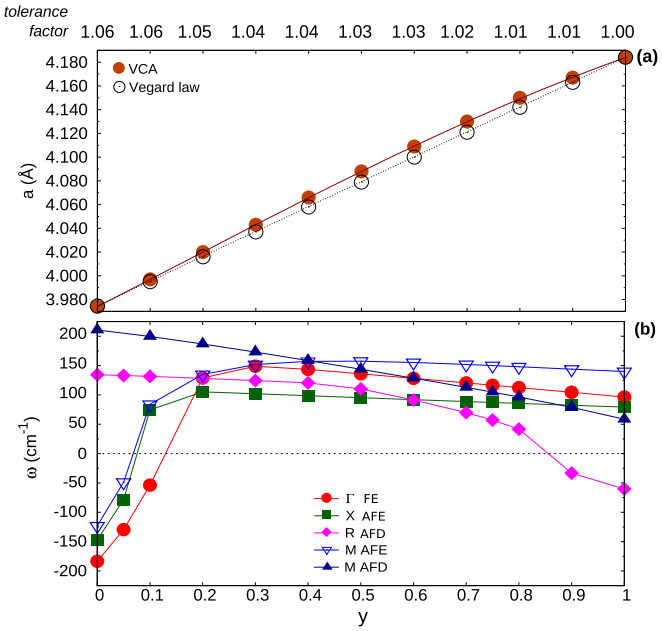

FIG. 9. (a) Evolution as a function of y composition in $BaTi_{1-y}Zr_yO_3$ of the cubic lattice parameter a_{cell} (in angstrom) relaxed within VCA. Vegard's law has been built on the theoretical values of the cubic $BaTiO_3$ and $BaZrO_3$ reported in Table I: $a(y) = (1 - y)a_{BTO} + (y)a_{BZO}$. (b) Trend of the lowest phonon frequencies (in cm^{-1}) at the high-symmetry points of the simple cubic Brillouin zone as a function of different y compositions.

concentration y, BTZ ceramics show relaxor properties. For $BaTi_{0.80}Zr_{0.20}O_3$ only one resonance of the permittivity at the ferroelectric-paraelectric T_C of about 315 K is observed, whereas for $y = 0.35$ the dielectric anomaly is broad and frequency-dependent as a function of temperature. Moreover, in Ref. [60], they provide an EXAFS study of BTZ systems and conclude that BTZ is relaxor and the average crystal structure is cubic ($Pm\bar{3}m$ space group) in the range $0.25 \leqslant y \leqslant 0.50$. In addition, in a complementary work on BCTZ [61], the x-ray diffraction has revealed (110) peaks in $BaTi_{0.80}Zr_{0.20}O_3$ ceramic but a weak tetragonality (i.e., $a/c \sim 1$), which means closeness to the cubic phase. However, no experimental data on single crystal samples are available for direct comparison with *ab initio* results.

As for the previous case of $(Ba,Ca)TiO_3$, we first investigate the $Ba(Ti,Zr)O_3$ system by means of the virtual crystal approximation. Then, we go beyond by using supercell-based calculations.

A. VCA approach

1. Lattice parameters

We first report the trend of the lattice parameter of the $Pm\bar{3}m$ cubic phase as a function of Zr-composition. Because of the bigger volume of $BaZrO_3$ with respect to $BaTiO_3$ (Table I), the trend is monotonically increasing with the amount of zirconium and the agreement with the linearity of the Vegard's law is quite satisfactory [Fig. 9(a)]. Contrariwise, because of the bigger ionic radius of Zr than Ti, the tolerance factor[1] decreases without going below 1, that is the value for pure $BaZrO_3$, as reported on top of Fig. 9.

2. Dynamical properties

Then, we focus on the dynamics by looking at the evolution of the lowest phonon frequencies at the high-symmetry points of the cubic Brillouin zone. Calculations have been performed on the VCA-optimized $Pm\bar{3}m$ structure. It results that the main effect of the Zr-doping is to abruptly stabilize the cubic phase, as clear from Fig. 9(b). In fact, already in the Ti-rich region, i.e., $y > 0.10$, the original polar instability vanishes and an AFD unstable mode $BaZrO_3$-like appears at the R-point only for $y \geqslant 0.90$. The reason behind such abrupt weakening of ferroelectricity in the BTZ "virtual-system" at low y-concentration can be traced back to abrupt changes in the type of interaction between the virtual cation at the B site and the oxygens. In fact, the total IFC along the B-O direction is of about -0.001 Ha/bohr^2 at $y \geqslant 0.05$. Therefore the change of sign with respect to the corresponding interaction in pure $BaTiO_3$ (Tables V) means that the Zr substitution strongly favors short-range repulsive forces.

Differently from BCT systems, it is not possible to relate such behavior to the evolution of the tolerance factor or to simple volumetric reasons. In fact, in line with the properties of the two parent compounds, t remains larger than one and the volume increases for each intermediate composition. The main mechanism involved here is the weakening of the Ti-O interaction when introducing Zr on the same B site, as this corresponds to either direct changes in the O $2p$ and B d hybridization mechanism from the electronic perspective or breaking correlated Ti-O chains necessary to sustain ferroelectricity in $BaTiO_3$ from the lattice dynamics. In fact, we have already seen in Sec. III A 4, that the Zr-O interaction in $BaZrO_3$ is strongly repulsive. Moreover, differently than the role played by $CaTiO_3$ in BCT, no contribution from the A site is observed, as the Ba-O interaction is too weak to sustain alone a polar instability in BTZ. As a consequence, it is finally not surprising that the "virtual"-BTZ system does not display any instabilities for a very large range of composition.

3. Energy landscape

In line with the drastic changes of the dynamical properties in BTZ predicted by VCA, the energy difference both between the three polar phases and with respect to the cubic one is abruptly reduced, as shown in Fig. 10. In fact, the energy competition is within 0.1 meV/f.u. at $y = 0.10$ and beyond this concentration no stable or metastable polar phases are allowed within VCA.

4. Polarization and piezoelectric response

After identifying the abrupt weakening of ferroelectricity in the BTZ virtual system, we now evaluate the associated effect on the piezoelectric response. Therefore we calculate the spontaneous polarization P_s and the piezoelectric coefficients

[1] Also in this case, we defined an average radius for the B cation as $\overline{r_B} = (1 - y)r_{Ti} + (y)r_{Zr}$

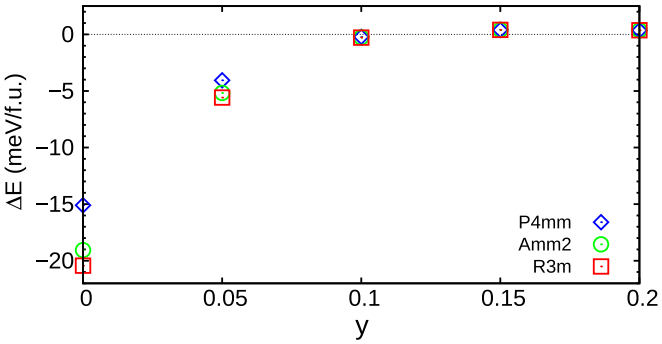

FIG. 10. Zoom on the evolution of the energy gain (in meV/formula unit) of the three polar structures relative to the cubic phase as a function of y-composition in the Ti-rich region within VCA.

d_{ij} for the stable phase, that is, the $R3m$ phase for $y = 0.05$ and 0.10 (Fig. 10). Also, in this case, as we are mostly interested in the qualitative trend of these properties as a function of Zr doping, we report values normalized to those of $R3m$ $BaTiO_3$.

In Fig. 11, we report values of P_s calculated both via Berry phase (blue circles) and Born effective charges (green rhombus). This is to be compared with the same calculations for BCT in Fig 7. In line with the strong weakening of the polar instability, P_s is drastically reduced by the Zr doping. Similarly to BCT, from further analysis of the distinguished contribution from effective charge variation and atomic displacements, it results that the evolution of P_s has to be widely ascribed to largely reduced atomic motions. However, by looking at $y = 0.10$, it is important to note that there is a disagreement between the value of polarization by fixing the Born effective charges to that of pure $R3m$ $BaTiO_3$ (red circles) or to the ones of $R3m$ BTZ virtual system (green rhombus) as the Zr doping also affects the Born effective charges. In fact, we have already shown that the Z^* associated to Zr is less anomalous than the one of Ti (Table III). Therefore the average effective charge associated to the "virtual" B cation is also reduced with increasing Zr concentration. This is an important warning about the ability of VCA in describing the properties arising from the mixing of Zr and Ti on the B site, as they have quite different electronic properties (see Sec. V C below).

Such decrease of P_s remains compatible with an increase of piezoelectricity. In fact, the huge increase of dielectric response ε_{ij}, associated to the drastic softening of the polar mode, largely compensates the decrease of P_s. This results in the enhancement of the piezoelectric response with respect to pure $BaTiO_3$, as reported in Fig. 11. Accordingly, the values of the lowest-frequency polar mode in the stable $R3m$ phase evolve like 169, 146, 69 (in cm^{-1}) for $y = 0.00$, 0.05, and 0.10, respectively.

As we see, the trends obtained from VCA are in reasonable agreement with the experimental observations. However, to understand the actual impact of the partial substitution of Ti with Zr on the dynamics of the system at the local level, supercell-based calculations are necessary.

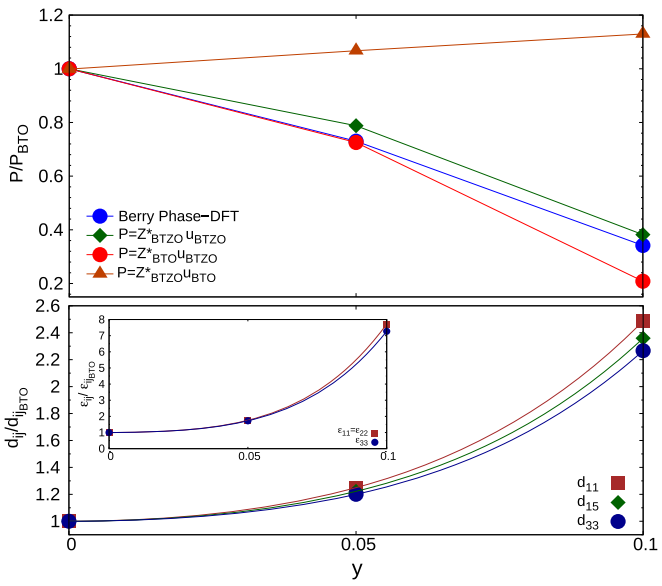

FIG. 11. Evolution of polarization, stress-free dielectric and piezoelectric coefficients in the rhombohedral-$R3m$ phase as a function of y composition in $BaTi_{1-y}Zr_yO_3$ within VCA. Values are normalized to the ones of $R3m$ $BaTiO_3$: $P_s^{BTO} \simeq 38$ $\mu C/cm^{-2}$; $d_{11}^{BTO} \simeq 76$, $d_{15}^{BTO} \simeq 270$ and $d_{33}^{BTO} \simeq 15$ pC/N; $\varepsilon_{11}^{BTO} \simeq 208$ and $\varepsilon_{33}^{BTO} \simeq 11$. (Top) Variation of the polarization as directly computed via Berry-phase calculations (blue closed circles) and via Born effective charges to disentangle the contribution of varying atomic charges and displacements. (Bottom) Trend of the d_{ij} coefficients and stress-free dielectric response ε_{ij}.

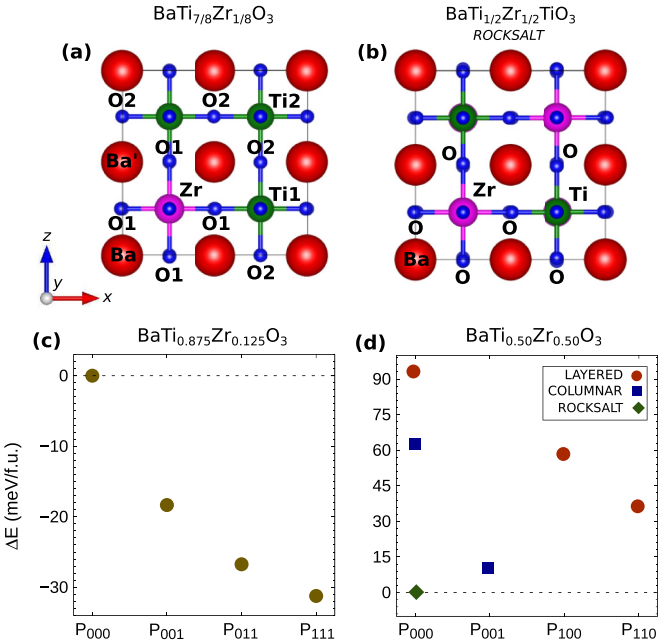

FIG. 12. Schematic representation of the atomic arrangement in $BaTi_{0.875}Zr_{0.125}O_3$ (a) and in rock-salt $BaTi_{0.50}Zr_{0.50}O_3$ (b). Labels help the visualization of the main atomic pair analyzed in Tables XI and XIII. Energy lowering (in meV/f.u.) with respect to the high-symmetry $Pm\bar{3}m$ phase for $BaTi_{0.875}Zr_{0.125}O_3$ (c) and with respect to high-symmetry rocksalt $Fm\bar{3}m$ configuration for $BaTi_{0.50}Zr_{0.50}O_3$ (d) as a function of different optimized polar states by means of supercells. The x-axis notation refers to the direction of the components of polarization.

TABLE XI. Interatomic force constants from VCA and supercell-based calculations for $BaTi_{0.875}Zr_{0.125}O_3$. Units are in Ha/bohr^2. Directions $xx'(\parallel)$, $yy'(\perp)$, and $zz'(\perp)$ refer to local coordinates system of the different pairs of atoms. Distances (in angstrom) between the selected atoms are also reported. Atoms' notation in the second column is consistent with Fig. 12(a).

$BaTi_{0.875}Zr_{0.125}O_3$									
	VCA				$2 \times 2 \times 2$ cell				
Atoms		Total	DD	SR	Atoms		Total	DD	SR
A-A'	($\parallel$)	−0.011	−0.006	−0.005	Ba-Ba′	($\parallel$)	−0.012	−0.006	−0.006
$d = 3.997$ Å	($\perp$)	+0.004	+0.003	+0.001	$d = 4.043$ Å	($\perp$)	+0.004	+0.003	+0.001
B-B'					Ti_1-Ti_2	(xx')	−0.068	−0.038	−0.029
$d = 3.997$ Å	($\parallel$)	−0.067	−0.037	−0.030	$d = 4.002$ Å	(yy')	+0.008	+0.018	−0.010
	($\perp$)	+0.009	+0.018	−0.011		(zz')	+0.008	+0.019	−0.011
					Ti_1-Zr	(xx')	−0.069	−0.034	−0.034
					$d = 4.002$ Å	(yy')	+0.008	+0.019	−0.011
						(zz')	+0.008	+0.019	−0.011
A-B					Ba-Ti_1	(xx')	−0.028	−0.022	−0.007
$d = 3.461$ Å	($\parallel$)	−0.030	−0.023	−0.008	$d = 3.478$ Å	(yy')	+0.014	+0.010	+0.003
	($\perp$)	+0.014	+0.011	+0.003		(zz')	+0.013	+0.011	+0.002
					Ba-Zr	(xx')	−0.031	−0.020	−0.011
					$d = 3.502$ Å	(yy')	+0.013	+0.011	+0.002
						(zz')	+0.013	+0.011	+0.002
B-O_1					Ti_1-O_1	($\parallel$)	−0.032	+0.239	−0.271
$d = 1.998$ Å					$d = 1.929$ Å	($\perp$)	−0.015	−0.052	+0.037
					Zr-O_1	($\parallel$)	−0.039	+0.199	−0.238
	($\parallel$)	−0.009	+0.229	−0.238	$d = 2.073$Å	($\perp$)	−0.013	−0.040	+0.027
	($\perp$)	−0.020	−0.045	+0.025	Ti_1-O_2	(xx')	+0.013	+0.239	−0.226
					$d = 2.012$ Å	(yy')	−0.023	−0.039	+0.016
						(zz')	−0.021	−0.046	+0.025
					Ti_2-O_2	($\parallel$)	+0.003	+0.244	−0.241
					$d = 1.990$ Å	($\perp$)	−0.021	−0.043	+0.022
A-O_1	(xx')	−0.001	+0.013	−0.014	Ba-O_1	(xx')	+0.000	+0.012	−0.011
$d = 2.826$ Å	(yy')	−0.005	−0.006	+0.002	$d = 2.860$ Å	(yy')	−0.010	−0.015	+0.005
	(zz')	−0.011	−0.016	+0.005		(zz')	−0.004	−0.006	+0.002

B. Supercell approach

In this section, we investigate the dynamical properties of $BaTi_{0.875}Zr_{0.125}O_3$ and $BaTi_{0.50}Zr_{0.50}O_3$ supercells. Structural details are provided in Sec. II C

1. $BaTi_{0.875}Zr_{0.125}O_3$

$BaTi_{0.875}Zr_{0.125}O_3$ supercell [Fig. 2(e)] hosts several instabilities in the cubic $Pm\bar{3}m$ phase, all related to ferroelectric and antiferroelectric distortions. The most unstable, with $\omega \simeq 214\text{i}$ cm^{-1}, is a polar mode mostly related to the opposite motion of Ti and O, while the Zr atom slightly moves in the same direction as the oxygens. The difference in these relative displacements affects the neighboring atom lying on the polar direction, that slightly moves with the oxygens as well. This means that, according to the labels indicated in Fig. 12(a), if the polar distortion is, for instance, along the x direction, Ti_1 slightly off-centers with Zr in the same direction as the oxygens, but opposite to the other Ti atoms. Ba atoms are almost fixed as in the parent $BaTiO_3$. Such different dynamics is made clear when looking at the interatomic force constants reported in Table XI. In fact, the original destabilizing Ti-O interaction of $BaTiO_3$ is not preserved for each direction in the system. The Ti-atoms having Zr as first neighbors experience a strong repulsive Ti-O interaction along the O-Zr-O-Ti-O chain direction, while the long-range forces remain the major ones along the other directions as well as for the other Ti atoms. This is strongly ascribed to the "chain-like" character of the polar instability of $BaTiO_3$, as discussed in Sec. III A 1: the polar instability requires a minimum number of correlated Ti-O displacements [25] that, however, are prevented along the chain containing Zr. In fact, according to the properties of $BaZrO_3$ described in Sec. III A 4, the Zr-O interaction remains strongly repulsive also in this Ti-rich solid solution. However, along the preserved O-Ti-O-Ti-O chains, the long-range interaction is even indirectly strengthened by the Zr presence. In fact, the bigger size of Zr (i.e., of the $[ZrO_6]$-octahedral volume) makes the Ti-O bond's length perpendicular to the O-Zr-O-Ti-O chain direction longer than in pure $BaTiO_3$. This mechanism locally favors the long-range interaction. Accordingly, the "on-site" force constants tensor associated to the Ti-atoms adjacent to Zr are anisotropic: by referring to Ti1 of Fig. 12(a), the "on-site"

TABLE XII. Lowest phonon frequencies (cm^{-1}) at the high-symmetry points of the tetragonal $P4/mmm$ Brillouin zone. As $BaTi_{0.5}Zr_{0.5}O_3$ has no instabilities within VCA, only results from supercells are reported.

	$BaTi_{0.5}Zr_{0.5}O_3$($P4/mmm$ supercell)					
Configuration	Γ(000)	Z (0 0 $\frac{1}{2}$)	M ($\frac{1}{2}$ $\frac{1}{2}$ 0)	A ($\frac{1}{2}$ $\frac{1}{2}$ $\frac{1}{2}$)	R (0 $\frac{1}{2}$ $\frac{1}{2}$)	X (0 $\frac{1}{2}$ 0)
layered [110]	274.18i	271.42i	65.17i	60.85i	259.90i	262.65i
columnar [001]	304.05i	90.60	301.88i	75.43	76.32	299.40i

terms are (+0.247,+0.132,+0.132) Ha/bohr^2. Therefore they are much more stiffer along the Zr direction, while softer along the transversal directions than in $BaTiO_3$ (see Table IV). The other Ti atoms display a slightly anisotropic tensor, but similar to the one in $BaTiO_3$: by referring to Ti2 of Fig. 12(a), values are (+0.162, + 0.151, + 0.162) Ha/bohr^2. In contrast, Zr displays an isotropic $BaZrO_3$-like tensor with diagonal values of about +0.229 Ha/bohr^2, as it experiences the same interactions in each direction. Concerning Ba at the A site, the dynamics is the same as in pure $BaTiO_3$. In fact, the A-O interatomic force constant is close to zero along parallel direction of the coupling meaning that Ba distortion does not lead ferroelectricity in $BaTi_{0.875}Zr_{0.125}O_3$. The A-B interaction is also similar to the one in the two parent compounds reported in Table V.

Such complex dynamics results in slightly reduced total polarization and more spread energy landscape with respect to the case of the parent $BaTiO_3$. On one hand, the calculated spontaneous polarization is of about 28 and 35 $\mu C/cm^2$ for the $P4mm$ and $R3m$ phases, respectively, while it is of about 34 and 38 $\mu C/cm^2$ for the corresponding phases in pure $BaTiO_3$. This has to be assigned to the local depolarizing contribution arising from the O-Zr-O-Ti-O chain. On the other hand, the energy gain of the three polar phases relative to the cubic phase is higher than in $BaTiO_3$ and it appears much more pronounced for the $Amm2$ and $R3m$ phases as reported in Fig. 12(c). This effect traces back to the overall volume increase, which further favors the rhombohedral phase.

2. $BaTi_{0.50}Zr_{0.50}O_3$

The case of $BaTi_{0.50}Zr_{0.50}O_3$ [Figs. 2(f)–2(h)] clearly reveals the importance of the atomic ordering on the dynamical properties. The first result is that the atomic arrangement associated to the high-symmetry $Fm\bar{3}m$ rocksalt configuration is lower in energy than the ordered $P4mmm$ structures based on chains or layers of same type of B cations: the three structures have been optimized and the energy lowering with respect to the highest energy layered configuration is of about −30.95 meV/f.u. for the columnar configuration and −93.73 meV/f.u. for the rocksalt.

Beyond that, all the three configurations show very different dynamical properties. Looking at the phonon frequencies reported in Table XII, unstable modes appear at each high-symmetry point of the $P4mmm$-tetragonal Brillouin zone of the layered-based supercell. Specifically, the two instabilities appearing at the M and A points are associated to antiferrodistortive modes due to oxygen rotations, while all the other instabilities are related to the polar instability arising from Γ and mostly ascribed to the (Ti,O)-polar motion along the direction of preserved O-Ti-O-Ti-O chains. Zr displays the same dynamics as described for the $BaTi_{0.875}Zr_{0.125}O_3$ case. Within the columnar configuration, the instabilities appear only along the Γ-X-M line and are linked to the polar distortion arising from the Γ-point with the same character as the former cases. In sharp contrast, no instability appears for the rocksalt configuration. In particular, the absence of O-Ti-O-Ti-O chain in any direction makes the cubic phase stable. As reported in Table XIII, in fact, both the Ti-O and Zr-O interactions are dominated by the short-range forces and the slightly destabilizing interaction between Ba and O atoms is not enough to globally destabilize the system.

Since the Zr doping directly affects the B-O interaction, the system clearly prefers to keep an isotropic surrounding environment in order to preserve the same kind of interaction in each direction, i.e., O-Zr-O-Ti-O chains like in the $Fm\bar{3}m$ structure. This arrangement prevents the original Ti-driven polar distortion of $BaTiO_3$. Therefore the ground state for the $y = 0.50$ composition is globally nonpolar, as reported in Fig. 12(d).

TABLE XIII. Interatomic force constants from supercell calculations for $BaTi_{0.50}Zr_{0.50}O_3$ in the cubic-$Fm\bar{3}m$ phase. Units are in (Ha/bohr^2). Directions (∥),(xx') and (⊥),(yy'),(zz') refer to the local coordinates system between different atomic coupling. Distances in angstrom between the selected atoms are also reported. Atomic labels refer to Fig. 12(b).

$BaTi_{0.50}Zr_{0.50}O_3$			
2 × 2 × 2 cell - $Fm\bar{3}m$			
	Atoms		Total
B-B'	Ti-Zr	(∥)	−0.063
	d = 4.075Å	(⊥)	+0.008
A-B	Ba-Ti	(∥)	−0.027
	d = 3.529 Å	(⊥)	+0.013
	Ba-Zr	(∥)	−0.030
	d = 3.529 Å	(⊥)	+0.013
B-O	Ti-O	(∥)	−0.002
	d = 1.978 Å	(⊥)	−0.020
	Zr-O	(∥)	−0.025
	d = 2.097 Å	(⊥)	−0.015
A-O	Ba-O	(xx')	+0.002
	d = 2.882 Å	(yy')	−0.011
		(zz')	−0.005

C. VCA versus supercell approaches

By comparing the results reported in Secs. V A and V B, it becomes clear that the VCA method is not suitable for describing the $Ba(Ti,Zr)O_3$ solid solutions. The decrease of polarization for increasing Zr concentration is obtained in both cases. However, within VCA, neither the energetics nor the dynamical properties are well reproduced. In particular, VCA does not detect any instability in the cubic phase already for $y > 0.10$, whereas it is not the case as found out in $BaTi_{0.875}Zr_{0.125}O_3$ supercell as well as in the experiments introduced at the beginning of the present section. As already widely discussed, the reason behind such failure is that VCA does not allow to access distinct contributions to the dynamics arising from the different nature of the mixed cations as well as the effects due different atomic ordering. The latter is, in fact, the main variable controlling the dynamics in BTZ. Additionally, we know that the FE instability in $BaTiO_3$ is strongly sensitive to the O $2p$-Ti $3d$ hybridization. Therefore, as Zr occupies $4d$ states, the changes in the electronic properties induced by the Zr doping directly affect the dynamics of the system. As such, the way VCA combines the different electronic properties from the parents $BaTiO_3$ and $BaZrO_3$ is also determinant in the failure of the VCA approach for BTZ.

In Fig. 13, we compare the electronic density of states (DOS) within the two approaches. It appears that VCA acts in making an "horizontal" average of the DOS of the parent compounds. This is clearly visible in Fig. 13(a), where we have aligned the valence-band maximum of $BaTiO_3$, $BaZrO_3$ and the VCA compound. In fact, the DOS calculated by VCA is the one of $BaTiO_3$ horizontally shifted toward that of $BaZrO_3$ proportionally to the 12.5% composition of Zr since it is linearly interpolating between the $3d$ states of Ti and $4d$ states of Zr. In Fig. 13(b), we reproduce this average by adding up the density of peaks facing one with the other with the weight fixed by the chosen composition. The result, plotted on top of the VCA graph, reproduces nicely the calculated DOS (nonlinear effects play a minor role in the creation of fictitious virtual atom).

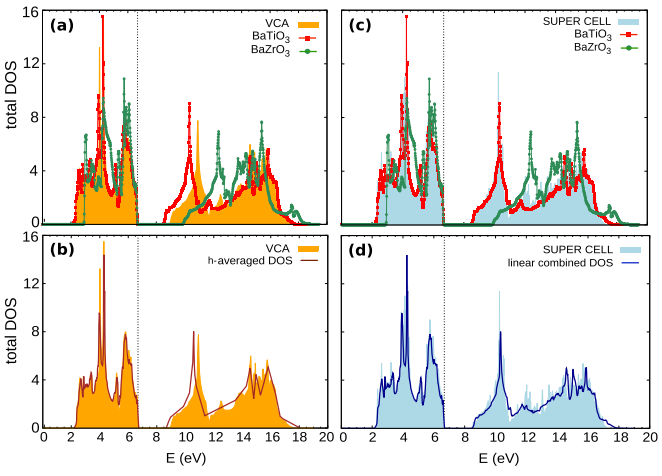

FIG. 13. Calculated electronic density of states for $BaTiO_3$, $BaZrO_3$, and $BaTi_{0.875}Zr_{0.125}O_3$. (Top) DOS of the BTZ solid solution as obtained within VCA (left) and supercell calculation (right) in comparison with the parent compounds. (Bottom) Empirical reproduction of DOS as obtained from "horizontal" average to reproduce the VCA (left) and linear combination for the supercell case (right).

The way supercell-based calculations combine properties from the parent compounds is significantly different [Fig. 13(c)]. It results to be a straightforward linear combination of the two DOS. In Fig. 13(d), we just added up $\frac{7}{8}DOS_{BTO} + \frac{1}{8}DOS_{BZO}$ and the plot perfectly overlaps the supercell calculated one.

This distinct way of averaging the electronic properties can be the reason why the two approaches reproduce different ground state for the same composition. The incorrect average location of the d states of the virtual atoms in VCA (i.e., at higher energy) prevents the correct p-d hybridization, which is at the basis of the ferroelectric distortion in $BaTiO_3$.

D. Role of cation arrangement

Since the dynamics in $Ba(Ti,Zr)O_3$ is strongly related to the geometrical and atomic ordering while the polar distortion in $BaTiO_3$ requires correlated displacements along (Ti,O) chains, we find it interesting to explore more deeply different compositions and cations arrangements. Thus we have performed additional calculations for idealized $BaZrO_3/BaTiO_3$ (BZO/BTO) supercells (Fig. 14) in order to clarify the role played by the geometrical environment and composition in getting ferroelectricity and homogeneous polarization in $Ba(Ti,Zr)O_3$ solid solutions.

At first, we considered a given structural ordering with different composition. We built $1 \times 1 \times L$ superlattices (BZO/mBTO) by adding up to six layers of $BaTiO_3$ to one unit cell thick layer of $BaZrO_3$, as represented in Fig. 14(a). This corresponds to decreasing concentrantion of zirconium from 50% for $L = 2$, to 33% for $L = 3$, 25% for $L = 4$, 20% for $L = 5$, and 17% for $L = 6$. The total length in terms of unit cells is $L = m + 1$. Then, proceeding from the evolution with L of the energetics and polarization along the stacking

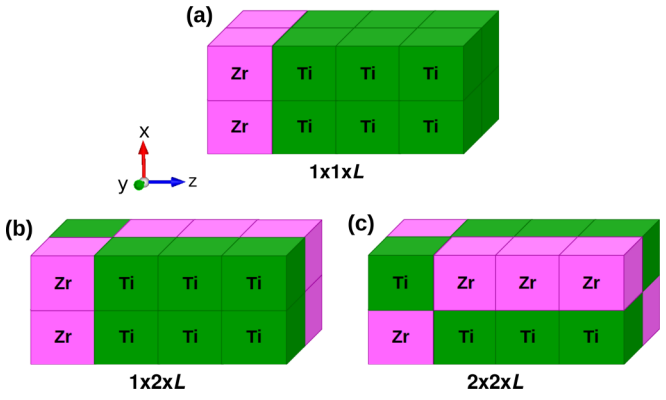

FIG. 14. Scheme of the investigated BZO/mBTO-based supercells. (a) $1 \times 1 \times L$ superlattice based on one single chain of $BaZrO_3$-$m$$BaTiO_3$ with decreasing composition of zirconium. The smallest chain with $L = 2$ corresponds to the layered 50% composition. The represented chain is doubled along the x and y direction to help the visualization of the crystal periodicity. [(b) and (c)] $1 \times 2 \times L$ and $2 \times 2 \times L$ supercells based on alternating chains $BaZrO_3$-$m$$BaTiO_3$ and $BaTiO_3$-$n$$BaZrO_3$ to keep a 50% global composition. The smallest cells with $L = 2$ correspond to the columnar and rocksalt 50% composition, respectively. The represented $1 \times 2 \times L$ case is doubled along the x to help visualization.

TABLE XIV. Comparison of P (in $\mu C/cm^2$) and d_{33} (in pC/N) as a function of the length L in the three investigated atomic arrangements, as obtained by Berry-phase and DFPT calculations. For $1 \times 1 \times L$ and $2 \times 2 \times L$ supercells, DFPT calculations have been performed only for $L = 3$. For comparison, in $P4mm$ $BaTiO_3$, we obtained $d_{33} \simeq 43.3$ pC/N. Relative energy gain between the optimized ferroelectric and paraelectric phases [ΔE(FE-PE) in meV/f.u.] is also reported.

	$1 \times 1 \times L$			$1 \times 2 \times L$			$2 \times 2 \times L$		
L	ΔE	P	d_{33}	ΔE	P	d_{33}	ΔE	P	d_{33}
2	0.0	0.0	0.0	0.0	0.0	0.0	0.0	0.0	0.0
3	−1.0	17.0	77.3	−0.8	10.2	34.0	−1.3	11.1	28.0
4	−4.2	24.2	57.2	−5.6	15.9	–	−9.2	17.3	–
5	−6.7	27.2	52.3	−10.2	18.1	–	−16.3	19.7	–
6	−8.6	28.9	49.7	−13.8	19.3	–	−21.7	21.0	–

direction, we tried to explain the appearance of ferroelectricity by a simple electrostatic model.

In detail, we started our study by investigating the appearance of polarization along the epitaxy direction of the $1 \times 1 \times L$ superlattice. For each length L, we fully relaxed the centrosymmetric $P4/mmm$ and the polar $P4mm$ structures, where the inversion symmetry breaking is due to the atomic displacements along the z direction. As expected, we found no polar distortions along the z direction for $L = 2$. Because of the periodicity of the crystal, this configuration corresponds, in fact, to the layered structure described in Sec. V B 2, Fig. 2. Conversely, for $L \geqslant 3$, the polar structures have an energy gain with respect to the paraelectric one and values of polarization increase with the number m of $BaTiO_3$ layers. Values of P_s are reported in Table XIV and in Fig. 16. Then we described the atomic distortion from the paraelectric to the ferroelectric phase as a cooperative motion around the center of mass (CM) of the system, in order to better clarify the driving mechanism. This description has revealed the active role of Zr atom in the polarization against the dynamical properties found out in bulk $BaZrO_3$ as well as in the investigated Ba(Ti,Zr)O_3 solid solutions (Secs. III A 4 and V B, respectively). For $m \geqslant 2$, BZO/mBTO superlattice behaves like $BaTiO_3$ with the opposite motion of the O anions and (Ti,Zr) cations. In terms of stiffness, the zirconium atom experiences a much smaller "on-site" force constant in the direction of the epitaxy, i.e., of the Ti atoms, that allows for the Zr-polar motion. Moreover, the associated Born effective charge, of about $\simeq 7.2e$, is considerably anomalous along that direction and comparable to that of Ti.

For the sake of completeness, we also performed DFPT calculations in order to evaluate the d_{33} piezoelectric coefficient in the $P4mm$ phase. Results are reported in Table XIV. It appears that this polar phase is not the ground state. In fact, it still presents phonon polar instabilities (not shown) in the (x,y) plane, i.e., along the preserved Ti-O-Ti-O chains, with dynamical properties similar to the Ba(Ti,Zr)O_3 solid solutions described in Sec. V B.

In order to interpret the latter results, specifically the polar activation of Zr, here we adapt the simple model proposed in Ref. [62] describing the behavior of dielectric/ferroelectric multilayers to our BZO/mBTO superlattice. Neglecting interface corrections, the total energy of a $(1,m)$ superlattice can be written as

$$E(P_{BZO}, P_{BTO}; m) = U_{BZO}(P_{BZO}) + mU_{BTO}(P_{BTO}) + C(m)(P_{BTO} - P_{BZO})^2. \quad (1)$$

Here, P is the polarization arising from the displacement of the ions from their high-symmetry positions under the condition of zero electric field, U is the internal energy of bulk $BaZrO_3$ and $BaTiO_3$ at zero field as a function of P and $C(m)(P_{BTO} - P_{BZO})^2$ is macroscopic electrostatic energy, E_{elec}, resulting from the eventual presence of nonvanishing electric fields in the layer when P_{BZO} and P_{BTO} are different. This term typically acts as an energy penalty which tends to reduce the polarization mismatch in polarizing the dielectric layer and depolarizing the ferroelectric one. In practice, when the dielectric layer is sufficiently polarizable, this term forces the system to adopt a uniform polarization along the stacking direction (z direction in Fig. 14), i.e., $P_{BZO} = P_{BTO} = P$. In this case, the model reduces to [63–65]

$$E(P; m) = U_{BZO}(P) + mU_{BTO}(P). \quad (2)$$

The energies $U_{BTO}(P)$ and $U_{BZO}(P)$ can be directly obtained from appropriate DFT calculations on bulk compounds. In the case of $BaTiO_3$, we built the adiabatic path from the paraelectric to the ferroelectric $P4mm$ phase (discussed in Sec. III B) by means of linear interpolation of the atomic displacements. During this interpolation the volume is fixed to the one of the polar structure. For each intermediate configuration, we computed the internal energy and polarization. This results into a double-well energy profile that we fit with the standard polynomial expansion

$$U_{BTO}(P) \simeq \alpha_T P^2 + \beta_T P^4 + \gamma_T P^6,$$

where α_T, β_T, and γ_T are the fitting parameters.[2] We used a similar expansion for $BaZrO_3$. However, according to the paraelectric nature of this compound, the coefficient of the second order term is positive. Thus we restricted the expansion to the fourth order and we write

$$U_{BZO}(P) \simeq \alpha_Z P^2 + \beta_Z P^4.$$

In this case, as the system does not show any polar instability, the only way to follow the evolution of the internal energy $U_{BZO}(P)$ with the ferroelectric distortion is to freeze the pattern of the motion along the z direction. We defined the total distortion τ as a linear combination of the eigendisplacements associated to the polar modes, i.e., $\tau = a_1\eta_{TO_1} + a_2\eta_{TO_2} + a_3\eta_{TO_3}$, with $\sum_i a_i^2 = 1$ and $\langle \eta_i | M | \eta_i \rangle = 1$. The first approach was to determine the coefficients of the expansion by minimizing $U_{BZO}(P)$ to equilibrium values of η_i with the constrain of fixed P, as proposed in Ref. [66]. From this minimization we obtained $a_1 = 0.945$, $a_2 = 0.325$, and $a_3 = 0.044$, that corresponds to a pattern dominated by the softest TO_1 mode of $BaZrO_3$ driven by the Ba motion (see

[2]The sixth-order term is introduced to ensure a proper description of the physics of the system as it is close to a tricritical point, i.e., change of the order of the phase transition via a change in sign of the coefficient of the fourth-order term

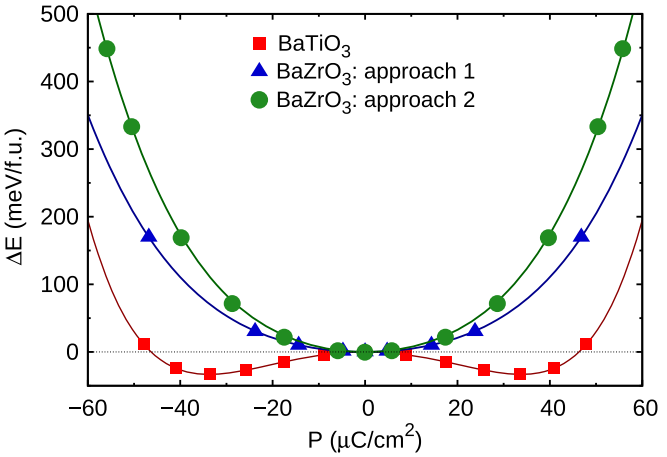

FIG. 15. Variation of total energy (in meV/f.u.) as a function of the varying polarization (in μC/cm^2) from the centric to the polar configurations for distorted bulk $BaTiO_3$ (red squares) and $BaZrO_3$. For the latter, curves as obtained within the two approaches are reported: (blue triangles) from the minimization procedure at fixed P; (green circles) from the relaxed pattern of distortion of $1 \times 1 \times 3$ superlattice.

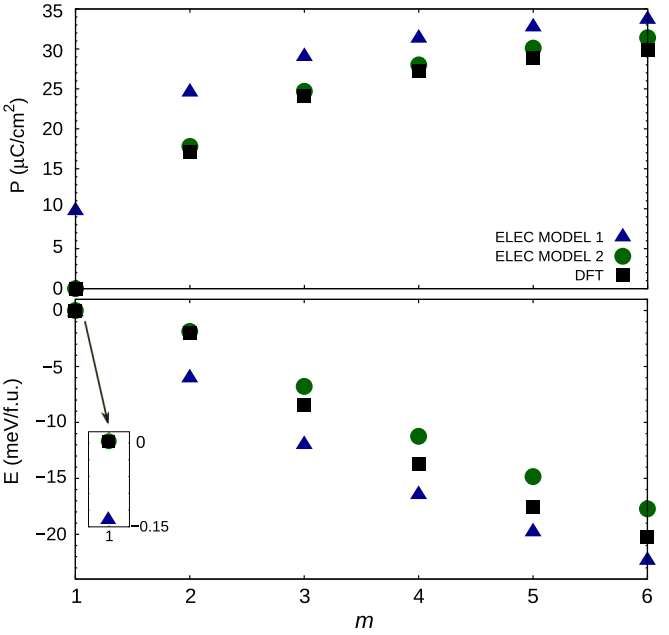

FIG. 16. Evolution of the total polarization (in μC/cm^2) and energy (in meV/formula unit) as a function of increasing number m of BTO layers. Values obtained from DFT calculations and from the electrostatic model are reported. We refer to results coming from the first approach based on the minimization at fixed P as model 1, while to those based on the relaxed pattern as model 2. The inset shows the different energies for $m = 1$. The E from DFT calculations refers to the relative energy gain between the optimized ferroelectric phase and the centrosymmetric reference with volume fixed to that of the polar structure.

Table III). However, this result is not in full agreement with the pattern of distortion obtained from the atomic relaxation in the superlattice previously described. Therefore we also built $U_{BZO}(P)$ from the relaxed pattern. In detail, we considered the distortion of the $BaZrO_3$ unit cell in the $1 \times 1 \times 3$ superlattice and we projected it on each TO_i mode in order to get the a_i coefficient to be compared with the previous procedure. We obtained $a_1 = 0.595$, $a_2 = 0.802$, and $a_3 = 0.051$, that clearly reveal the key role of zirconium. The $U_{BZO}(P)$ curves obtained via the two procedures are shown in Fig. 15.

Then, from the minimization of Eq. (2) with respect to P, we obtain that a spontaneous polarization is admitted if the condition $m > \frac{\alpha_Z}{|\alpha_T|}$ is satisfied, otherwise P is zero. The resulting formula for the polarization and energy are

$$P^2(\alpha,\beta,m) \simeq -\frac{m\alpha_T + \alpha_Z}{2(m\beta_T + \beta_Z)},$$

$$E(\alpha,\beta,m) \simeq -\frac{(m\alpha_T + \alpha_Z)^2}{4(m\beta_T + \beta_Z)}.$$

Coefficients are reported in Table XV. The evolution of P and E resulting from the electrostatic model within the two different approaches and from DFT calculations are reproduced in Fig. 16. The two models globally reproduce the same trend, however the second one built on the relaxed pattern is in better agreement with the calculations. In fact, from the parameters related to the first curve, with smaller curvature, a polar state is admitted for all m instead of the condition $m \geqslant 2$. On one hand, the quantitative inconsistencies between the two approaches, both in the distortion pattern and in ferroelectric properties of the superlattice, point out that a simple model only based on pure bulk quantities can fail in reproducing the dynamics of the system because of strong coupling between the two different B cations at play. On the other hand, the perfect agreement obtained between the "second" model and first-principles calculations (Fig. 16) confirms the validity of the hypothesis of uniform P in the superlattice, i.e., electrostatic energy cost equal to zero, due to the fact that the polar distortion of Zr preserves the charge transfer along Zr-O-Ti-O-Ti-O chains. Moreover, P asymptotically approaches the value of $P4mm$ $BaTiO_3$, that is of about $\simeq$34 μC/cm^2 as calculated via DFT.

TABLE XV. Values of the parameters used in the $U_{BTO}(P)$ and $U_{BZO}(P)$ expansion as resulted from a fitting procedure. For $BaZrO_3$, we reports the parameters for both the constructions: (a) from the minimization procedure at fixed P (blue curve in Fig. 15) and (b) from the empirical approach (green curve in Fig. 15).

	$BaTiO_3$			$BaZrO_3$		
α_T	β_T	γ_T	$\alpha_Z^{(a)}$	$\beta_Z^{(a)}$	$\alpha_Z^{(b)}$	$\beta_Z^{(b)}$
−0.054	1.8×10^{-5}	3.4×10^{-9}	0.048	1.37×10^{-5}	0.073	2.26×10^{-5}

These results, in particular the cooperative $BaTiO_3$-like atomic motion along the Zr-O-Ti-O-Ti-O chains, are the manifestation of the "chainlike" nature of the distortion. In fact, we already discussed in Sec. V B how the break of correlated Ti-O chains introduced by the polar inactive Zr prevents the propagation of the original $BaTiO_3$ distortion in Ba(Ti,Zr)O_3 solid solutions. Nevertheless, when a minimum number of consecutive Ti atoms are preserved along those chains, the substitution of one atom of Ti with one of Zr does not suppress the polarization. On the contrary, the electrostatic coupling forces the system to sustain a homogeneous P by making Zr polar active.

Previous calculations and physical interpretation have been based on superlattices with decreasing Zr concentration. Therefore, in order to further prove the crucial role played by the local "chainlike" correlation over the increasing BTO-concentration, we have better distinguished the effects arising from the composition and from the imposed atomic ordering. Thus we carried DFT calculations on $1 \times 2 \times L$ and $2 \times 2 \times L$ ordered supercells as we did for the $1 \times 1 \times L$ case. These two supercells, composed by alternating single chains of BZO/mBTO and BTO/nBZO, allow to keep the total composition fixed to 50% of Zr and Ti and to preserve locally the imposed "chain-like" atomic ordering, as reproduced in Figs. 14(b) and 14(c).

For both the arrangements, it is not surprising to get no polar phases for $L = 2$ from the inversion symmetry breaking along the z direction. In fact, by periodicity, these structures correspond to the columnar and rocksalt orders described in Sec. V B 2, Fig. 2. Relevant results arise from $L \geqslant 3$, since a spontaneous polarization appears along the BZO/mBTO chains driven by the (Zr,Ti) motion against the oxygens inside the global $BaTi_{0.50}Zr_{0.50}O_3$ matrix. As in the $1 \times 1 \times L$ superlattice, in fact, we described the atomic displacements as a cooperative motion around CM and we found out that most of the polar distortion comes from the B cations stacked on the local BZO/mBTO chains. We also obtained sizable d_{33} piezoelectric coefficient, but smaller than in the $1 \times 1 \times L$ and pure $P4mm$ $BaTiO_3$ cases, as reported in Table XIV (because of the high computational cost for these supercells, we performed DFPT calculations only for the case $L = 3$). A simple explanation could be that the coexistence of the BZO/mBTO and BTO/nBZO chains, that behave differently since the cations in the latter one do not participate to the polarization, could globally prevent the variation of P. Noteworthy is that the polar $P4mm$ phase within the $2 \times 2 \times L$ structure is stable.

The main finding from the comparison of results coming from the three different structures is the polar activation of zirconium in Ba(Ti,Zr)O_3 system as a function of specific atomic ordering, that is local BZO/mBTO chains with $m \geqslant 2$, and independent of the total composition of the matrix. Therefore, the analysis and physical interpretation of the dynamics conducted through the previous electrostatic model remains valid also for the $1 \times 2 \times L$ and $2 \times 2 \times L$ cases: Zr atom is locally activated by a Zr-Ti coupling to avoid polarization gradients and electrostatic energy cost. However, then, the gain of energy related to polarizing ferroelectric $BaTiO_3$ is decreased by the energy cost to polarize $BaZrO_3$.

From the $U(P)$ curves of the pure compounds in Fig. 15 and trends reported in Fig. 16, the maximum Zr-concentration to get a ferroelectric system seems to be around 30% in agreement with experimental observations. Beyond this concentration, the results are line with the observed relaxor behavior of $BaTi_{1-y}Zr_yO_3$ and existence of polar nanoregions associated to local fluctuation of y, that allows for correlated polar motions, as described in Refs. [67–69,71]. Maiti *et al.*, in their experimental investigation of the correlation between structure and property in Ba(Ti,Zr)O_3 ceramics [67,70], point out that a gradual incorporation of Ti^{4+} into the nonpolar $BaZrO_3$ lattice results in the evolution of relaxation behavior because of the increasing amount of ordering and density of nano-sized Ti^{4+}-rich polar regions in the Zr^{4+}-rich matrix. Moreover, C. Laulhé *et al.* suggest that the observation of such polar nanoregions consist in 1D-chains with correlated Ti displacements [69]. By means of Monte Carlo simulations, Akbarzadeh *et al.* describe the Ti sites as nuclei acting to formation of polar clusters with rather small contribution from Zr sites [71].

Accordingly, by means of combined DFT calculations and phenomenological model, we have provided a complementary microscopic information. In particular, the behavior of the polar clusters in a global paraelectric matrix, like the case of the investigated $BaTi_{0.50}Zr_{0.50}O_3$ composition, can due to the cooperative motion of Zr and Ti atoms and not only by isolated Ti dipoles.

VI. DISCUSSION

Properties of (Ba,Ca)TiO_3 and Ba(Ti,Zr)O_3, discussed in Secs. IV and V, can be better understood in relationship with those of the pure $BaTiO_3$, $CaTiO_3$, $CaZrO_3$, and $BaZrO_3$ parent compounds discussed in Sec. III. In fact, these two solid solutions result from the mixing of systems with very different dynamics. This turns out to be a crucial point regarding the suitableness of the *ab-initio* method employed, VCA vs direct supercell calculations.

When going from $BaTiO_3$ to $CaTiO_3$ in (Ba,Ca)TiO_3, the main feature is the mixing of the so called B-driven and A-driven ferroelectricity associated to the two parent compounds, respectively. Cubic $BaTiO_3$, in fact, exhibits strong and highly polar instabilities that expand over the entire Γ-X-M planes of the Brillouin zone, as shown in Fig. 3(a). They are determined by the destabilizing Ti-O interaction resulting in the relative motion of Ti atoms with respect to oxygens. Particularly, this polar distortion requires cooperative atomic displacements along Ti-O chains. From the electronic point of view, such instability is ascribed to the hybridization between the O $2p$ and Ti $3d$ states [48]. The sizable stiffness of Ba determines its negligible contribution to the distortion instead. Related values of the "on-site" and interatomic force constants are reported in Tables IV and V. These mechanisms stabilize the rhombohedral $R3m$-phase, as reported in Fig. 4. On the contrary, $CaTiO_3$, in its cubic phase, hosts a strong polar instability confined at Γ and mostly related to a polar motion of Ca and O. In fact, we found that a strong destabilizing interaction occurs between these two atoms (Table V). Such Ca driven instability is ascribed to steric effects as the smaller size and greater softness

of Ca than Ba (Tables I and IV). In fact, same dynamical properties characterize also $CaZrO_3$ where the covalency between Zr and O is even further reduced [48]. Moreover, the associated reduced volume of $CaTiO_3$ with respect to $BaTiO_3$ makes the Ti-O interaction mainly repulsive and Ti atoms much more stiffer. These mechanisms favor the tetragonal $P4mm$ phase over the $R3m$ one. However, the ground state is determined by the strong AFD instabilities present along the M-R line. See Figs. 3(b) and 4. Accordingly, as obtained from supercell calculations for $BaTiO_3$-rich compositions, the mixing of the two A cations in $Ba_{1-x}Ca_xTiO_3$ solid solutions does not make barium active in the polar distortion, but introduces a cooperative motion of Ca-atoms together with Ti atoms against the oxygens cage. In particular, a ferroelectric ground state is predicted up to $x = 0.50$. Such prediction, has been achieved within both supercell-based and VCA approaches. Moreover, interesting trends in (Ba,Ca)TiO_3 are achievable within this approximation. In fact, as it is expected from the dynamical properties and energetics of the two parent compounds, the increasing Ca-composition favors $P4mm$-like polar phases over the $R3m$ one. In the Ba-rich region, this behavior makes the three ferroelectric states very close in energy and gives rise to increasing piezoelectric response as the energy landscape in terms of polarization orientation becomes more and more isotropic (Figs. 6 and 7). These properties actually occur for $Ba_{0.875}Ca_{0.125}TiO_3$, as obtained from the use of supercells. However, within VCA, the distinction of the dynamics of Ba and Ca atoms is not accessible, because only a final average effect from the two cations at the A site is reproduced, as shown in Fig. 5(c). This method forces the change of character of the mechanisms at play without allowing distinction of the opposite nature of Ba and Ca. In fact, Ca is actually polar active for each x. Such limitation is evident in the polarization trend, that is decreasing with Ca concentration within VCA, while it is increasing within the supercells, and in the finding of the concentration where the inversion of polar phases takes place.

When going from $BaTiO_3$ to $BaZrO_3$ in Ba(Ti,Zr)O_3, the scenario is completely different. $BaZrO_3$, in fact, does not host any polar instability. Zr atom is quite stiff and the Zr-O interaction is strongly repulsive, as reported in Tables IV and V. From the electronic point of view, this can be ascribed to the fact that Zr occupies $4d$ states less hybridized with the $2p$ states of O. Therefore, at first, low Zr doping further stabilizes the $R3m$ phase in $BaTi_{1-y}Zr_yO_3$ because of the larger ionic radius of Zr than Ti. However, the spontaneous polarization is slightly reduced. Then, for higher Zr-concentration, the system tends to globally reduce the polar distortion. In fact, the presence of Zr on the B-site introduces breaks along the correlated Ti-O-Ti-O chains, by preventing the preservation of polarization. Such mechanisms are evident both for $y = 0.125$ and $y = 0.50$ supercells compositions. For instance, in $BaTi_{0.50}Zr_{0.50}O_3$, the energetically favored $Fm\bar{3}m$ rocksalt configuration is stable. Nevertheless, ferroelectricity can be locally preserved in Ti-rich regions. Moreover, by building different supercell environments based on $BaZrO_3/mBaTiO_3$ chains, we found that as soon as Zr experiences at least two subsequent Ti atoms, it becomes active in the polarization and a cooperative motion of the two B cations is observed. The reason of such behavior, explained via a basic electrostatic model, is that Zr is locally activated in order to preserve homogeneous polarization along the Zr-O-Ti-O-Ti-O chain and to minimize the electrostatic energy cost. Such important role played by local structures on the Zr-Ti coupling and differences in the electronic configuration of the two B cations make VCA not suitable for the Ba(Ti,Zr)O_3 system. In fact, predictions achieved via supercell-based calculations concerning both the dynamics and energetics are not reproduced by VCA.

In both (Ba,Ca)TiO_3 and Ba(Ti,Zr)O_3, we found that the two types of cations introduced at the A and B sites, respectively, behave very differently and can therefore hardly be described by the same averaged virtual atom. Although providing some trends, VCA is therefore not suitable for reproducing and understanding the microscopic physics of (Ba,Ca)(Ti,Zr)O_3 solid solutions. This clarifies why recent attempts [72] to study BCTZ from a VCA-based effective Hamiltonian required to adjust by hands some of the parameters initially fitted from first principles in order to reproduce experimental data.

VII. CONCLUSIONS

We have investigated the dynamical properties of chosen compositions of (Ba,Ca)(Ti,Zr)O_3 solid solutions and the four parent compounds by means of first-principles calculations. In (Ba,Ca)TiO_3, the competition between the B-type and the A-type ferroelectricity of the two parent compounds is the key mechanism behind the eventual competition between different polar phases. In fact, $BaTiO_3$ and $CaTiO_3$ have a reversed energy sequence of ferroelectric states so that a crossover between them is required to achieve the inversion. The achievement of such crossover enhances the piezoelectric response. Additionally, we have predicted the existence of a ferroelectric ground state characterized by a cooperative (Ca,Ti) motion at least up to the 50% composition of the solid solution.

Different behavior characterizes Ba(Ti,Zr)O_3, where the appearance of ferroelectricity is strongly dependent on the local atomic arrangements and composition. Although the cubic phase is highly stable for $BaZrO_3$, by the use of a simple electrostatic model, we found out that the presence of (Zr,mTi)-chains favors correlation of polar distortions in order to preserve an homogeneous polarization along the chain. As a consequence, even if a ferroelectric ground state can be observed up to the critical concentration of 30% of zirconium, polar nanoregions can be locally preserved for larger concentrations.

From a methodological point of view, we have provided a direct comparison between the virtual crystal approximation (VCA) and direct supercell calculations. We have demonstrated that the specific microscopic physics of the (Ba,Ca)TiO_3 and Ba(Ti,Zr)O_3 solid solutions imposes severe limitations to the applicability of the virtual crystal approximation. By construction, this approximation fails at reproducing both specific local arrangements and the same-site independent motion of the active atoms involved in the ferroelectric instabilities. Also, it oversimplifies the actual electronic band structure of the doped systems. These are key features for the overall behavior of $BaTiO_3$-based solid solutions that need to be addressed by means direct supercell calculations. We

think that our findings establish a solid guideline for further investigations in understanding more deeply properties of the interesting (Ba,Ca)(Ti,Zr)O_3 solid solutions and in designing new lead-free piezoelectrics.

ACKNOWLEDGMENTS

This work is supported by the European project EJD-FunMat 2015, program H2020-MSCA-ITN-2014, under the Marie Sklodowska-Curie Grant Agreement No. 641640. Calculations have been performed on the Céci facilities funded by F.R.S-FNRS (Grant No. 2.5020.1) and on the Tier-1 supercomputer of the Fédération Wallonie-Bruxelles funded by the Walloon Region (Grant No. 1117545). D.A. would like to thank Matthieu Jean Verstraete, Eric Bousquet, Fabio Ricci, Alexandre Martin, and Alain Mercy for useful discussions and technical support. Ph.G. acknowledges support of the F.R.S.-FNRS Hit4FiT project and of the ARC project AIMED.

[1] Directive 2002/95/EC, Off. J. Eur. Un. **L37**, 19 (2003); Directive 2011/65/EU, *ibid.* **L174**, 88 (2011).
[2] R. C. Kell and N. J. Hellicar, Acta Acust. United Ac. **6**, 235 (1956).
[3] D. Berlincourt and H. Jaffe, Phys. Rev. **111**, 143 (1958).
[4] W. Liu and X. Ren, Phys. Rev. Lett. **103**, 257602 (2009).
[5] D. S. Keeble, F. Benabdallah, P. A. Thomas, M. Maglione, and J. Kreisel, Appl. Phys. Lett. **102**, 092903 (2013).
[6] H. Fu and R. E. Cohen, Nature (London) **403**, 281 (2000).
[7] M. Acosta, N. Khakpash, T. Someya, N. Novak, W. Jo, H. Nagata, and G. A. Rossetti, and J. Rödel, Phys. Rev. B **91**, 104108 (2015).
[8] K. Brajesh, M. Abebe, and R. Ranjan, Phys. Rev. B **94**, 104108 (2016).
[9] Ph. Ghosez, E. Cockayne, U. V. Waghmare, and K. M. Rabe, Phys. Rev. B **60**, 836 (1999).
[10] X. Gonze and C. Lee, Phys. Rev. B **55**, 10355 (1997).
[11] X. Gonze, J.-M. Beuken, R. Caracas, F. Detraux, M. Fuchs, G.-M. Rignanese, L. Sindic, M. Verstraete, G. Zerah, F. Jollet, M. Torrent, A. Roy, M. Mikami, Ph. Ghosez, J.-Y. Raty, and D. C. Allan, Comput. Mater. Sci. **25**, 478 (2002).
[12] X. Gonze, G.-M. Rignanese, M. Verstraete, J.-M. Beuken, Y. Pouillon, R. Caracas, F. Jollet, M. Torrent, G. Zerah, M. Mikami, Ph. Ghosez, M. Veithen, J.-Y. Raty, V. Olevano, F. Bruneval, L. Reining, R. Godby, G. Onida, D. R. Hamann, and D. C. Allan, Z. Kristallog. **220**, 558 (2005).
[13] X. Gonze, B. Amadon, P.-M. Anglade, J.-M. Beuken, F. Bottin, P. Boulanger, F. Bruneval, D. Caliste, R. Caracas, M. Cote, T. Deutsch, L. Genovese, Ph. Ghosez, M. Giantomassi, S. Goedecker, D. R. Hamann, P. Hermet, F. Jollet, G. Jomard, S. Leroux, M. Mancini, S. Mazevet, M. J. T. Oliveira, G. Onida, Y. Pouillon, T. Rangel, G.-M. Rignanese, D. Sangalli, R. Shaltaf, M. Torrent, M. J. Verstraete, G. Zerah, and J. W. Zwanziger, Computer Phys. Comm. **180**, 2582 (2009).
[14] Z. Wu and R. E. Cohen, Phys. Rev. B **73**, 235116 (2006).
[15] D. R. Hamann, Phys. Rev. B **88**, 085117 (2013).
[16] L. Bellaiche and D. Vanderbilt, Phys. Rev. B **61**, 7877 (2000).
[17] Ph. Ghosez, D. Desquesnes, X. Gonze, and K. M. Rabe, AIP Conf. Proc. **535**, 102 (2000).
[18] J. W. Edwards, R. Speiser, and H. L. Johnston, J. Am. Chem. Soc **73**, 2934 (1951).
[19] A. R. Akbarzadeh, I. Kornev, C. Malibert, L. Bellaiche, and J. M. Kiat, Phys. Rev. B **72**, 205104 (2005).
[20] R. Ali and M. Yashima, J. Solid State Chem. **178**, 2867 (2005).
[21] R. W. G. Wyckoff, *Crystal Structures* (Interscience Publishers, New York, 1964), Vol. 2, p. 390.
[22] A. F. Devonshire, Philos. Mag. **40**, 1040 (1949); **42**, 1065 (1951); Adv. Phys. **3**, 85 (1954).
[23] W. Cochran, Adv. Phys. **9**, 387 (1960).
[24] W. Zhong, D. Vanderbilt, and K. M. Rabe, Phys. Rev. B **52**, 6301 (1995).
[25] Ph. Ghosez, X. Gonze, and J.-P. Michenaud, Ferroelectrics **206**, 205 (1998).
[26] Y. Qi, S. Liu, I. Grinberg, and A. M. Rappe, Phys. Rev. B **94**, 134308 (2016).
[27] G. Shirane, H. Danner, and R. Pepinsky, Phys. Rev. **105**, 856 (1957).
[28] A. W. Hewat, Ferrelectrics **6**, 215 (1974).
[29] G. H. Kwei, A. C. Lawson, S. J. L. Billinge, and S. W. Cheong, J. Phys. Chem. **97**, 2368 (1993).
[30] W. Zhong and D. Vanderbilt, Phys. Rev. Lett. **74**, 2587 (1995).
[31] B. J. Kennedy, C. J. Howard, and B. C. Chakoumakos, J. Phys.: Condens. Matter **11**, 1479 (1993).
[32] Y. Wang and R. C. Liebermann, Phys. Chem. Minerals **20**, 147 (1993).
[33] Z. F. Hou, Physica B **403**, 2624 (2008).
[34] P. Stoch, J. Szczerba, J. Lis, D. Madej, and Z. Pedzich, J. Eur. Ceram. Soc **32**, 665 (2012).
[35] Y. Du, Z. P. Jin, and P. Y. Huang, J. Am. Ceram. Soc **75**, 3040 (1992).
[36] Ph. Ghosez, X. Gonze, and J.-P. Michenaud, Ferroelectrics **194**, 39 (1997).
[37] X. Gonze, J.-C. Charlier, D. C. Allan, and M. P. Teter, Phys. Rev. B **50**, 13035 (1994).
[38] W. Zhong, R. D. King-Smith, and D. Vanderbilt, Phys. Rev. Lett. **72**, 3618 (1994).
[39] A. M. Glazer, Acta Crystallogr. B **28**, 3384 (1972).
[40] S. Amisi, E. Bousquet, K. Katcho, and Ph. Ghosez, Phys. Rev. B **85**, 064112 (2012).
[41] L. Bellaiche, and J. Íñiguez, Phys. Rev. B **88**, 014104 (2013).
[42] N. A. Benedek and C. J. Fennie, J. Phys. Chem. C **117**, 13339 (2013).
[43] N. Miao, N. C. Bristowe, B. Xu, M. J. Verstraete, and Ph. Ghosez, J. Phys.: Condens. Matter **26**, 035401 (2014).
[44] X. Cheng and M. Shen, Mater. Res. Bull. **42**, 1662 (2007).
[45] D. Fu and M. Itoh, arXiv:1503.00406 [cond-mat.mtrl-sci], 2015.
[46] V. D. Araújo, F. V. Motta, A. P. A. Marques, C. A. Paskocimas, M. R. D. Bomio, E. Longo, and J. A. Varela, J. Mater. Sci. **49**, 2875 (2014).
[47] R. D. Shannon, Acta Cryst. A **32**, 751 (1976).
[48] R. E. Cohen and H. Krakauer, Phys. Rev. B **42**, 6416 (1990).
[49] Ph. Ghosez, X. Gonze, and J.-P. Michenaud, Europhys. Lett. **33**, 713 (1996).
[50] E. Bousquet, and Ph. Ghosez, Phys. Rev. B **74**, 180101 (2006).

[51] R. D. King-Smith and D. Vanderbilt, Phys. Rev. B **47**, 1651 (1993).
[52] Ph. Ghosez, J.-P. Michenaud, and X. Gonze, Phys. Rev. B **58**, 6224 (1998).
[53] F. Cordero, Materials **8**, 8195 (2015).
[54] K. M. Rabe, and Ph. Ghosez, Topics Appl. Phys. **105**, 117 (2007).
[55] J. W. Bennett, I. Grinberg, and A. M. Rappe, Chem. Mater. **20**, 5134 (2008)
[56] I. Levin, V. Krayzman, and J. C. Woicik, Appl. Phys. Lett. **102**, 162906 (2013).
[57] J. Ravez and A. Simon, Eur. J. Solid State Inorg. Chem. **34**, 1199 (1997).
[58] J. Savez, C. Broustera, and A. Simon, J. Mater. Chem. **9**, 1609 (1999).
[59] A. Simon, J. Ravez, and M. Maglione, J. Phys.: Condens. Matter **16**, 963 (2004).
[60] C. Laulhé, F. Hippert, J. Kreisel, M. Maglione, A. Simon, J. L. Hazemann, and V. Nassif, Phys. Rev. B **74**, 014106 (2006).
[61] V. S. Puli, D. K. Pradhan, B. C. Riggs, D. B. Chrisey, and R. S. Katiyar, Integrated Ferrolectrics **157**, 139 (2014).
[62] Ph. Ghosez, and J. Junquera, *Handbook of Theoretical and Computational Nanotechnology*, (American Scientific, Stevenson Ranch, CA, 2006), Chap. 5
[63] M. Dawber, C. Lichtensteiger, M. Cantoni, M. Veithen, Ph. Ghosez, K. Johnston, K. M. Rabe, and J.-M. Triscone, Phys. Rev. Lett. **95**, 177601 (2005).
[64] M. Dawber, N. Stucki, C. Lichtensteiger, S. Gariglio, Ph. Ghosez, and J.-M. Triscone, Adv. Mater. **19**, 4153 (2007).
[65] E. Bousquet, J. Junquera, and Ph. Ghosez, Phys. Rev. B **82**, 045426 (2010).
[66] N. Sai, K. M. Rabe, and D. Vanderbilt, Phys. Rev. B **66**, 104108 (2002).
[67] T. Maiti, R. Guo, and A. S. Bhalla, J. Am. Ceram. Soc. **91**, 1769 (2008).
[68] J. Kreisel, P. Bouvier, M. Maglione, B. Dkhil, and A. Simon, Phys. Rev. B **69**, 092104 (2004).
[69] C. Laulhé, F. Hippert, J. Kreisel, A. Pasturel, A. Simon, J.-L. Hazemann, R. Bellissent, and G. J. Cuello, Phase Transition **84**, 438 (2011).
[70] N. K. Karan *et al.*, J. Raman Spectrosc. **40**, 370 (2009).
[71] A. R. Akbarzadeh, S. Prosandeev, Eric J. Walter, A. Al-Barakaty, and L. Bellaiche, Phys. Rev. Lett. **108**, 257601 (2012).
[72] Y. Nahas, A. Akbarzadeh, S. Prokhorenko, S. Prosandeev, R. Walter, I. Kornev, J. Íñiguez, and L. Bellaiche, Nat. Commun. **8**, 15944 (2017).
[73] K. Momma and F. Izumi, J. Appl. Crystallogr. **44**, 1272 (2011).